JOURNAL OF APPLIED CRYSTALLOGRAPHY

ISSN 1600-5767

Received 31 July 2024
Accepted 14 February 2025

Edited by P. Munshi, Shiv Nadar Institution of Eminence, Delhi NCR, India

Keywords: cocrystals; Rietveld refinement; NMR crystallography; multinuclear NMR; mechanochemistry.

Supporting information: this article has supporting information at journals.iucr.org/j

Rietveld refinement and NMR crystallographic investigations of multicomponent crystals containing alkali metal chlorides and urea

Cameron S. Vojvodin,[a,b] Sean T. Holmes,[a,b] Christine E. A. Kirschhock,[c] David A. Hirsh,[d] Igor Huskić,[e] Sanjaya Senanayake,[f] Luis Betancourt,[f] Wenqian Xu,[g] Eric Breynaert,[c,h] Tomislav Friščić[e,i] and Robert W. Schurko[a,b]*

[a]Department of Chemistry and Biochemistry, Florida State University, Tallahassee, FL 32306, USA, [b]National High Magnetic Field Laboratory, Tallahassee, FL 32310, USA, [c]Centre for Surface Chemistry and Catalysis – Characterisation and Application Team, KU Leuven, 3001 Leuven, Belgium, [d]Department of Chemistry and Biochemistry, University of Windsor, Windsor, Ontario N9B 3P4, Canada, [e]McGill University, Montreal, Quebec H3A 0B8, Canada, [f]Chemistry Division, Brookhaven National Laboratory, Upton, NY 11973, USA, [g]X-ray Science Division, Advanced Photon Source, Argonne National Laboratory, Argonne, IL 60439, USA, [h]NMR/X-ray platform for Convergence Research (NMRCoRe), KU Leuven, 3001 Leuven, Belgium, and [i]School of Chemistry, University of Birmingham, Edgbaston, Birmingham B15 2TT, United Kingdom. *Correspondence e-mail: rschurko@fsu.edu

New mechanochemical preparations of three multicomponent crystals (MCCs) of the form *M*Cl:urea·*x*H_2O (*M* = Li, Na and Cs) are reported. Their structures were determined by an NMR crystallography approach, combining Rietveld refinement of synchrotron powder X-ray diffraction data (PXRD), multinuclear (^{35}Cl, ^{7}Li, ^{23}Na and ^{133}Cs) solid-state NMR (SSNMR) spectroscopy and thermal analysis. The mechanochemical syntheses of the three MCCs, two of which are novel, were optimized for maximum yield and efficiency. ^{35}Cl SSNMR is well suited for the structural characterization of these MCCs since it is sensitive to subtle differences and/or changes in chloride ion environments, providing a powerful means of examining H···Cl^- bonding environments. Alkali metal NMR is beneficial for identifying the number of unique magnetically and crystallographically distinct sites and enables facile detection of educts and/or impurities. In the case of NaCl:urea·H_2O, ^{23}Na magic-angle spinning NMR spectra are key, both for identifying residual NaCl educt and for monitoring NaCl:urea·H_2O degradation, which appears to proceed *via* an autocatalytic decomposition process driven by water (with a rate constant of $k = 1.22 \times 10^{-3}$ s^{-1}). SSNMR and PXRD were used to inform the initial structural models. Following Rietveld refinement, the models were subjected to dispersion-corrected plane-wave density functional theory geometry optimizations and subsequent calculations of the ^{35}Cl electric field gradient tensors, which enable the refinement of hydrogen-atom positions, as well as the exploration of their relationships to the local hydrogen-bonding environments of the chloride ions and crystallographic symmetry elements.

1. Introduction

An active area of research in crystal engineering is the synthesis, characterization and rational design of multi-component crystals (MCCs), including cocrystals, salts, hydrates and their permutations (Jones *et al.*, 2006; Babu & Nangia, 2011; Cherukuvada *et al.*, 2016; Gadade & Pekamwar, 2016; Mir *et al.*, 2019). Pharmaceutical cocrystals are an important class of MCCs, consisting of at least one active pharmaceutical ingredient (API) and one or more pharmaceutically acceptable coformers (Karimi-Jafari *et al.*, 2018; Luedeker *et al.*, 2016). Pharmaceutical cocrystals are increasingly important in the pharmaceutical industry since it is possible to design products rationally to exhibit specific

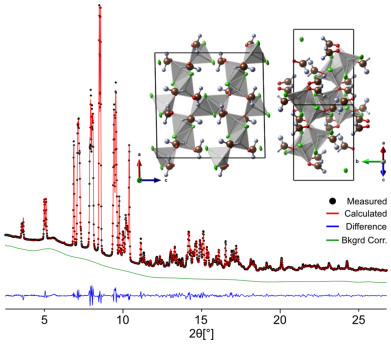

physicochemical properties (*e.g.* stability, solubility, bioavailability and tableting behaviour) with careful consideration of coformers and synthetic methods (McNamara *et al.*, 2006; Kuminek *et al.*, 2016; Weyna *et al.*, 2009; Friščić & Jones, 2010). Ionic cocrystals involving metal halides (*e.g.* LiCl, NaCl, KCl *etc.*) are excellent candidates for designing new solid forms of neutral APIs (*e.g.* they might not contain ionizable functional groups) since they offer additional ways to enhance and tailor physicochemical properties. Consequently, there is a need for reaction strategies and techniques for rapidly generating high yields of phase-pure MCCs and/or pharmaceutical cocrystals comprising diverse constituents, alongside reliable methods for their characterization.

'Mechanochemistry' encompasses a class of techniques that employ mechanical actions (*e.g.* rubbing, grinding or shearing) to induce chemical and/or physical transformations, typically involving solid reactants (Friščić *et al.*, 2020; Howard *et al.*, 2018; Tan & García, 2019). In recent years, mechanochemistry has established itself as an important synthetic tool for the production of a wide variety of materials, including organic crystals, metal–organic frameworks and pharmaceuticals (Friščić *et al.*, 2020; Howard *et al.*, 2018; Margetić & Štrukil, 2016). A common mechanochemical method is ball milling, where solid reactants (or educts) and ball bearings are placed in a sealed milling jar, which is agitated using a mechanical vibration or rotation stage to induce a reaction. Ball milling can involve neat grinding (NG), where the dry solid reactants are ground together, or liquid-assisted grinding (LAG) (Friščić *et al.*, 2009), where a small amount of liquid (often a microlitre quantity) is added to increase reaction efficiency, act as a catalyst and/or prepare novel solid forms unobtainable by conventional synthetic pathways (Friščić & Jones, 2010; Howard *et al.*, 2018; Tan & García, 2019; James *et al.*, 2012; Andersen & Mack, 2018; Tan *et al.*, 2016; Tan & Friščić, 2018). Mechanochemistry has garnered much interest due to its adherence to the tenets of 'green' chemistry, including minimal solvent use, low energy input, high atom economy, and reduced waste and/or by-products (Howard *et al.*, 2018; James *et al.*, 2012; Tan & Friščić, 2018; Varma, 2014; Baig & Varma, 2012).

The characterization of solid forms emerging from mechanochemical reactions is essential for identifying and determining the structures of products or by-products and/or the presence of residual educts. Since these solids are often microcrystalline powders, single-crystal X-ray diffraction (SCXRD) is not feasible. There are many alternative techniques for their characterization, including powder X-ray diffraction (PXRD), thermogravimetric analysis (TGA), differential scanning calorimetry (DSC), vibrational spectroscopy (IR and Raman) and solid-state NMR (SSNMR) spectroscopy (Weyna *et al.*, 2009; Cerreia Vioglio *et al.*, 2017; Pindelska *et al.*, 2017). In particular, if high-quality PXRD data can be acquired it is possible to determine crystal structures *via* Rietveld refinement. However, there are numerous challenges associated with Rietveld refinement, including sample quality, data quality (*e.g.* signal-to-noise ratio, limited angular ranges, systematic errors), peak overlap from multiple phases, the selection of an appropriate refinement model (*e.g.* space group, atomic positions *etc.*), the choice of refinement constraints for convergence and the need for a proficient level of expertise in crystallography (McCusker *et al.*, 1999; Buchsbaum & Schmidt, 2007; Toby, 2006). Since SSNMR can give detailed information on the molecular-level structure, local environments and even interatomic proximity, it is well positioned as a complementary technique to aid in the crystallographic characterization of products of mechanochemical reactions.

NMR crystallography (NMRX) is a broad term describing the combined use of SSNMR spectroscopy, X-ray diffraction (XRD) methods and quantum chemical calculations to solve, validate and/or refine crystal structures (Leroy & Bryce, 2018; Bryce, 2017; Martineau, 2014; Martineau *et al.*, 2014; Harris *et al.*, 2009; Ashbrook & McKay, 2016; Taulelle, 2009; Hodgkinson, 2020). Most modern NMRX studies rely on comparisons of experimentally measured chemical shifts (commonly ^{1}H, ^{13}C and ^{15}N) with those obtained from theory, both to guide the solution of crystal structures and to assess crystal structure quality (Baias *et al.*, 2013; Widdifield *et al.*, 2020; Watts *et al.*, 2016; Hartman *et al.*, 2016; Holmes *et al.*, 2020; Bryce & Sward, 2006; Schurko & Jaroszewicz, 2015; Wu & Zhu, 2012; Yates *et al.*, 2005; Pawlak *et al.*, 2013; Soss *et al.*, 2017; Kalakewich *et al.*, 2015; Abraham *et al.*, 2011). Although chemical shifts can be measured with relative ease, they are often challenging and time consuming to calculate accurately from first principles, making them of limited use for NMRX studies in certain cases (*e.g.* chemical shift tensors that are only marginally impacted by their longer-range environment).

Measurements and first-principles calculations of quadrupolar interaction (QI) parameters can provide an alternative route for NMRX (Rice *et al.*, 2020; Romao *et al.*, 2015; Martineau *et al.*, 2012; Widdifield *et al.*, 2015; Klein *et al.*, 2022; Peach *et al.*, 2018; Hildebrand *et al.*, 2014; Hamaed *et al.*, 2008; Holmes *et al.*, 2022*a*; Holmes *et al.*, 2022*b*; Burgess *et al.*, 2014). SSNMR spectra of quadrupolar ($I > 1/2$) nuclei almost always feature powder patterns that are strongly influenced by the QI. With careful experimentation, it is possible to measure not only the isotropic chemical shift (δ_{iso}) but also the quadrupolar coupling constant (C_Q) and asymmetry parameter (η_Q), which can be compared with electric field gradient (EFG) tensors derived from computations (see Table 1 for definitions). EFG tensors are exquisitely sensitive to subtle changes or differences in solid-state structures, including weaker long-range interactions (*e.g.* hydrogen bonding, π–π stacking and halogen bonding), thereby providing a source of structural information distinct from chemical shifts in both origin and scope (Schurko & Jaroszewicz, 2015; Wu & Zhu, 2012; Hildebrand *et al.*, 2014; Moudrakovski, 2013; Bryce *et al.*, 2001; Burgess *et al.*, 2012; Xu *et al.*, 2016; Szell & Bryce, 2016*a*). Moreover, density functional theory (DFT) calculations of EFG tensors are much less computationally expensive than those of chemical shift (CS) tensors, which could aid in accelerating NMRX routines. As such, it is desirable to develop and employ quadrupolar NMR crystallography (QNMRX) for structure validation and refinement, NMRX-guided Rietveld refinements (Harris,

Table 1
Experimental and calculated ^{7}Li, ^{23}Na, ^{133}Cs and ^{35}Cl EFG and CS tensors.

The experimental uncertainties in the last digit for each value are indicated in parentheses. Parameters indicated with a dash '–' are not applicable or have little to no effect on the simulated ^{35}Cl SSNMR.

Material	Nucleus		C_Q† (MHz)	η_Q†	δ_{iso}‡ (ppm)	Ω‡ (ppm)	κ‡	α§ (°)	β§ (°)	γ§ (°)
NaCl:urea·H_2O	^{35}Cl	Exp.	1.37 (5)	0.73 (8)	4 (2)	75 (10)	−0.35 (8)	65 (5)	81 (2)	4 (3)
	^{35}Cl	Calc.¶	1.64	0.49	−15	83	−0.22	96	81	6
	^{23}Na	Exp.	1.99 (3)	0.29 (3)	4.1 (4)	–	–	–	–	–
	^{23}Na	Calc.	−2.08	0.43	2.2	10	0.50	30	19	47
CsCl:urea	^{35}Cl	Exp.	1.55 (3)	0.52 (3)	93 (1)	60 (10)	−0.72 (10)	5 (25)	28 (10)	84 (20)
	^{35}Cl	Calc.	−1.77	0.69	82	61	−0.83	0	90	90
	^{133}Cs	Exp.	0.106 (5)‖	0.09 (2)	137 (1)	220 (20)	−0.85 (15)	–	–	–
	^{133}Cs	Calc.	−0.112	0.00	57.9	88	−1.00	90	90	180
LiCl:urea	^{35}Cl	Exp.	2.63 (2)	0.85 (3)	4(3)	77 (20)	0.50 (10)	75 (15)	20 (10)	160 (20)
	^{35}Cl	Calc. (Cl1)	2.99	0.90	−10	78	0.80	80	86	143
	^{35}Cl	Calc. (Cl2)	2.94	0.90	−9.4	79	0.63	80	84	125
	^{7}Li	Exp.	0.093 (4)‖	0.84 (2)	0.69 (5)	–	–	–	–	–
	^{7}Li	Calc. (Li1)	−0.143	0.79	1.07	5	−0.29	123	87	182
	^{7}Li	Calc. (Li2)	−0.139	0.74	0.97	5	−0.24	306	86	179

† The principal components of the EFG tensors are ranked as $|V_{33}| \geq |V_{22}| \geq |V_{11}|$. The quadrupolar coupling constant and asymmetry parameter are defined as $C_Q = eQV_{33}/h$ and $\eta_Q = (V_{11} - V_{22})/V_{33}$, respectively, where e is the fundamental charge of an electron, Q is the quadrupolar moment and h is Planck's constant. The sign of C_Q cannot be determined from the experimental ^{35}Cl SSNMR spectra. ‡ The principal components of the chemical shift tensors are defined using the frequency-ordered convention such that $\delta_{11} \geq \delta_{22} \geq \delta_{33}$. The isotropic chemical shift, span and skew are given by $\delta_{iso} = (\delta_{11} + \delta_{22} + \delta_{33})/3$, $\Omega = \delta_{11} - \delta_{33}$ and $\kappa = 3(\delta_{22} - \delta_{iso})/\Omega$, respectively. § The Euler angles α, β and γ define the relative orientation of the EFG and CS tensors. Euler angles are reported using the $ZY'Z''$ convention (Adiga *et al.*, 2007; Pincherle, 1958; Mehring, 1983). ¶ Theoretical EFG and CS tensor parameters were obtained from calculations on structures refined at the RPBE-TS* level. ‖ Only an upper limit can be estimated from simulations, due to the small magnitudes of the experimental parameters.

2011; Lim *et al.*, 2011; Smalley *et al.*, 2022) and NMRX-assisted crystal structure prediction (Holmes *et al.*, 2020; Martineau *et al.*, 2012; Widdifield *et al.*, 2015; Peach *et al.*, 2018; Burgess *et al.*, 2014; Burgess *et al.*, 2012; Bonhomme *et al.*, 2012; Sene *et al.*, 2013; Alkan *et al.*, 2017; Johnston *et al.*, 2011).

Of the quadrupolar nuclides commonly found in organic solids, ^{35}Cl (I = 3/2) is among the most widely investigated, due to the relative ease of ^{35}Cl SSNMR experiments and prevalence of HCl salts of organic solids (Holmes *et al.*, 2022*b*; Bryce *et al.*, 2001; Szell & Bryce, 2016*b*; Hirsh *et al.*, 2016; Hirsh *et al.*, 2018; Vogt *et al.*, 2013; Namespetra *et al.*, 2016; Szell & Bryce, 2020; Peach *et al.*, 2018; Pandey *et al.*, 2016; Wijesekara *et al.*, 2020; Vojvodin *et al.*, 2022; Abdulla *et al.*, 2023; Hirsh *et al.*, 2019; Szell *et al.*, 2023; Bryce *et al.*, 2006). ^{35}Cl SSNMR spectra typically feature broad central-transition (CT, 1/2 ↔ −1/2) powder patterns that are influenced by the second-order quadrupolar interaction (SOQI) and chemical shift anisotropy (CSA). In particular, the ^{35}Cl EFG tensors of chloride ions are extremely sensitive to their local hydrogen-bonding environments, namely, the number of H···Cl^- hydrogen bonds, their H···Cl^- distances and their spatial arrangements (Hildebrand *et al.*, 2014; Hamaed *et al.*, 2008; Holmes *et al.*, 2022*a*; Holmes *et al.*, 2022*b*). Therefore, ^{35}Cl SSNMR spectra provide unique spectral fingerprints for each magnetically and crystallographically distinct chloride ion, enabling straightforward differentiation of polymorphs, hydrates and other solid forms, including MCCs (Peach *et al.*, 2018; Holmes *et al.*, 2022*a*; Holmes *et al.*, 2022*b*; Namespetra *et al.*, 2016; Vojvodin *et al.*, 2022; Abdulla *et al.*, 2023; Hirsh *et al.*, 2019).

Herein, we discuss the mechanochemical preparation of three urea-containing MCCs of the form *M*Cl:urea·$x$$H_2O$ (*M* = Li, Na or Cs; x = 0, 1). Urea is ideal for developing multi-nuclear QNMRX methods since it is a small and simple molecule capable of engaging in hydrogen bonding as both a donor and an acceptor, which has relevance in drug design and delivery for establishing drug–target interactions. We also present QNMRX characterizations using synchrotron PXRD, thermal analysis and multinuclear SSNMR, in tandem with Rietveld refinements and plane-wave DFT calculations. Novel mechanochemical syntheses of the three MCCs were optimized for maximum yield and efficiency. The identities and purities of all MCCs and educts were confirmed with PXRD and multinuclear SSNMR; in the case of NaCl:urea·H_2O, PXRD data were compared with simulated patterns derived from the previously reported SCXRD structure (Müller *et al.*, 2008). To aid the Rietveld refinements, all data were used in concert to inform the initial structural inputs. The final structural solutions were then subjected to dispersion-corrected plane-wave DFT geometry optimizations. Lastly, DFT calculations of the ^{35}Cl EFG tensors were conducted on the geometry-optimized structures to assess the agreement between experiment and theory and to elucidate the relationships between the NMR parameters and molecular-level structures.

2. Experimental

2.1. Materials

Alkali metal chlorides (*M*Cl, *M* = Li, Na, K, Rb and Cs), urea and solvents were purchased from Sigma Aldrich Ltd. Solid reagents were dried *in vacuo* (120°C, 15 mm Hg) for a minimum of 16 h before use.

2.2. Mechanochemical synthesis of MCCs

CsCl:urea and LiCl:urea were prepared mechanochemically *via* NG, whereas NaCl:urea·H_2O was prepared through LAG with 10 µl of triethylamine (TEA) used as the milling liquid

additive (η = 0.236 µl mg^{-1}) (full details are given in Table S1 in the supporting information). Syntheses were conducted using a Retsch Mixer Mill 400, 10 ml stainless steel milling jars, two 7 mm stainless steel ball bearings (ball weight 1.384 g), a milling frequency of 30 Hz and, in most cases, a total milling time of up to 40 min. Unless indicated otherwise, syntheses were scaled to a total weight of *ca* 200 mg for the solid reagents to ensure that the ball milling conditions were as similar as possible between different reactions.

2.3. TGA and DSC

Simultaneous TGA and DSC measurements were performed on a TA SDT Q600 instrument using an alumina crucible. Samples were heated from room temperature (23°C) to 500°C at a heating rate of 10°C min^{-1} under a dry argon purge (gas flow of 100 ml min^{-1}). Approximately 5 mg of sample was used for all measurements.

2.4. PXRD

The PXRD patterns were acquired using a Proto AXRD benchtop diffractometer with a Cu $K\alpha$ (λ = 1.540593 Å) radiation source and a Proto DECTRIS hybrid pixel detector. NaCl:urea·H_2O and CsCl:urea were mounted on a Proto plate sample holder, whereas LiCl:urea was mounted on an air-sensitive sample holder. All diffraction experiments were conducted with an X-ray tube voltage of 30 kV, a current of 20 mA, 2θ angles ranging from 5 to 50°, a step size of 0.015° and a dwell time of 5 s (resulting in an acquisition time of *ca* 35 min per sample). PXRD patterns were processed and simulated using the *CrystalDiffract* software package (https://www.crystalmaker.com).

2.5. Synchrotron XRD

High-resolution synchrotron PXRD patterns were collected on the ANL–APS beamline 17-BM at the Advanced Photon Source (APS) at Argonne National Laboratory (ANL). A NIST standard of lanthanum hexaboride (LaB_6) powder was used to calibrate the sample-to-detector distances (400, 700 and 1000 mm) and the synchrotron X-ray wavelength (λ = 0.45390 Å), and a flat Si detector (PerkinElmer) was used to collect two-dimensional XRD patterns. Samples were loaded into 1 mm (outer diameter, o.d.) Kapton tubes. All measurements were conducted at 22°C.

2.6. SSNMR spectroscopy

2.6.1. Overview

All moderate-field NMR experiments [B_0 = 9.4 T, ν_0(^{7}Li) = 155.51 MHz, ν_0(^{23}Na) = 105.84 MHz, ν_0(^{133}Cs) = 52.48 MHz, ν_0(^{35}Cl) = 39.21 MHz] were conducted on a Bruker Avance III HD NMR spectrometer with an Oxford 9.4 T wide-bore magnet at the University of Windsor. Static experiments were conducted using a Varian/Chemagnetics 4 mm triple-resonance HXY magic-angle spinning (MAS) probe, whereas MAS NMR experiments were conducted using a Varian/Chemagnetics 4 mm double-resonance HX MAS probe. Samples were packed in air-tight 4 mm o.d. zirconia rotors for both sets of experiments. MAS experiments were stabilized at 5°C using a Varian variable-temperature (VT) upper stack and nitrogen gas heat exchanger to prevent sample decomposition due to frictional heating in the rotor.

High-field NMR experiments [B_0 = 21.1 T, ν_0(^{35}Cl) = 88.14 MHz, ν_0(^{1}H) = 900.00 MHz] were conducted on a Bruker Avance II NMR spectrometer equipped with an Oxford 21.1 T standard-bore magnet at the National Ultrahigh-Field NMR Facility for Solids (Ottawa, Canada). Static experiments were performed using a static purpose-built 4 mm double-resonance HX low-*E* probe, whereas MAS NMR experiments were conducted using a 4 mm double-resonance HX MAS Bruker probe. All samples were packed in 4 mm o.d. zirconia rotors. MAS samples were cooled to 5°C using a Bruker BVT-3000 and dry nitrogen gas to prevent MAS heating and subsequent sample decomposition. Detailed acquisition parameters for all SSNMR experiments can be found in the supporting information (Table S2). All data were processed in Bruker *TopSpin* (Version 4.1.1; Bruker, 2020) and spectral fitting was carried out using the *ssNake* software package (van Meerten *et al.*, 2019). To ensure proper expression of the Euler angles (describing the relative orientation of the EFG and CS tensors) in the $ZY'Z''$ convention (Adiga *et al.*, 2007; Pincherle, 1958; Mehring, 1983), the results of simulations in *ssNake*, which uses the $ZX'Z''$ convention and different definitions for anisotropic chemical shift and quadrupolar parameters, were verified in *WSolids1* (Eichele & Wasylishen, 2021). Euler angles were converted from the $ZY'Z''$ convention for direct comparison with tensor orientations extracted from *CASTEP* calculations (see below) using the *EFGShield* software package (Adiga *et al.*, 2007), which uses the $ZY'Z''$ convention (Perras & Paterson, 2024). Uncertainties were assessed through bidirectional variation of each parameter *via* comparison of experimental and simulated spectra.

2.6.2. ^{7}Li SSNMR spectroscopy

^{7}Li MAS NMR spectra were acquired at 9.4 T using a rotor-synchronized Hahn-echo sequence (ν_{rot} = 5 kHz) and high-power ^{1}H decoupling (ν_2 = 25 kHz), with a 2.5 µs non-selective π/2 pulse (ν_1 = 100 kHz), an optimized recycle delay of 10 s and 1024 scans. Chemical shifts were referenced to 1.0 M LiCl(aq) in D_2O [δ_{iso}(^{7}Li) = 0.0 ppm].

2.6.3. ^{23}Na SSNMR spectroscopy

^{23}Na MAS NMR spectra were acquired at 9.4 T with Bloch decay and Hahn-echo pulse sequences, with ν_{rot} = 10 kHz, high-power ^{1}H decoupling (ν_2 = 50 kHz), 2.5 µs CT-selective π/2 pulses (ν_1 = 50 kHz), an optimized recycle delay of 25 s and 32 scans. Chemical shifts were referenced to 0.1 M NaCl(aq) in D_2O [δ_{iso}(^{23}Na) = 0.0 ppm]. To monitor the decomposition of NaCl:urea·H_2O MCCs, VT ^{23}Na MAS NMR spectra were collected with a recycle delay of 37.5 s and 16 scans, resulting in a total experiment time of 10 min. The integrated intensities of the powder patterns in the ^{23}Na MAS NMR spectra were used to monitor the decomposition of the MCC into the starting educts.

2.6.4. ^{133}Cs SSNMR spectroscopy

^{133}Cs MAS NMR spectra were acquired at 9.4 T with a rotor-synchronized Hahn-echo pulse sequence with a spinning speed of ν_{rot} = 5 kHz, no ^{1}H decoupling, 4.0 µs non-selective $\pi/2$ pulses (ν_1 = 62.5 kHz), an optimized recycle delay of 90 s and 32 scans. Chemical shifts were referenced to 1.0 M CsCl(aq) in D_2O [$\delta_{iso}(^{133}Cs)$ = 0.0 ppm].

2.6.5. ^{35}Cl SSNMR spectroscopy

^{35}Cl NMR spectra were acquired at B_0 = 9.4 and 21.1 T under static and MAS conditions. At 9.4 T, static and MAS (ν_{rot} = 12 kHz) spectra were acquired with a Hahn-echo sequence with high-power ^{1}H decoupling [$\nu_2(^{1}H)$ = 25 kHz]. At 21.1 T, static spectra were acquired with a quadrupolar echo sequence (90°–τ–90°–acq) with high-power ^{1}H decoupling [$\nu_2(^{1}H)$ = 35 kHz]. MAS spectra were acquired with a Bloch decay pulse sequence and ^{1}H decoupling [$\nu_2(^{1}H)$ = 25 kHz]. Chemical shifts were referenced to solid NaCl [$\delta_{iso}(^{35}Cl)$ = 0.0 ppm].

2.6.6. ^{35}Cl variable-temperature NMR

^{35}Cl VT NMR experiments were conducted on a Bruker NEO spectrometer with an Oxford 18.8 T narrow-bore magnet [$\nu_0(^{35}Cl)$ = 78.383 MHz] at the National High Magnetic Field Laboratory (NHMFL). Spectra were acquired with a purpose-built 5 mm HX static probe under static conditions (*i.e.* stationary samples) with samples packed into 5 mm polychlorotrifluoroethylene sample holders with Viton O-rings designed at the NHMFL and machined by Shenzhen Rapid Direct Co. Ltd. Spectra were acquired with a QCPMG pulse sequence employing CT-selective pulses, calibrated recycle delays at all temperatures and a continuous-wave (CW) ^{1}H decoupling field of 40 kHz. See Table S3 for further details. ^{35}Cl chemical shifts were referenced with respect to 0.1 M NaCl(aq) at $\delta_{iso}(^{35}Cl)$ = 0 ppm using NaCl(s) as a secondary reference at $\delta_{iso}(^{35}Cl)$ = −41.11 ppm.

2.7. DFT calculations

2.7.1. Overview

All quantum chemical calculations were performed within the framework of plane-wave DFT as implemented in the *CASTEP* module (Clark *et al.*, 2005) of *BIOVIA Materials Studio 2020* (https://www.3ds.com/products/biovia/materials-studio), with structural models derived from the Rietveld refinements presented herein (see Section 3.3 for details) or from single-crystal X-ray structures of LiCl, NaCl and CsCl (Ganesan & Girirajan, 1987; Cherginets *et al.*, 2006; Ievina *et al.*, 1938). All DFT calculations employed the RPBE functional (Hammer *et al.*, 1999), ZORA ultrasoft pseudopotentials generated on the fly (Yates *et al.*, 2007), and a version of the Tkatchenko and Scheffler dispersion correction force field (DFT-TS) (Tkatchenko & Scheffler, 2009), which was reparameterized (*i.e.* DFT-TS*) to aid in refining crystal structures of organic solids (Holmes *et al.*, 2020). The TS* semi-empirical dispersion correction was selected for this work because it is parameterized for elements up to and including the sixth period.

2.7.2. Geometry optimizations

Geometry optimization used the LBFGS energy minimization scheme (Pfrommer *et al.*, 1997) while holding the unit-cell parameters constant. Calculations used an SCF convergence threshold of 5×10^{-6} eV atom^{-1} and a plane-wave cut-off energy of 800 eV, and evaluated integrals over a Brillouin zone using a Monkhorst–Pack grid with *k*-point spacing of 0.05 Å^{-1} (Monkhorst & Pack, 1976). Structural convergence was determined using a maximum change in energy of 5×10^{-6} eV atom^{-1}, a maximum displacement of 5×10^{-4} Å atom^{-1} and a maximum Cartesian force of 10^{-2} eV Å^{-1}.

2.7.3. NMR interaction tensors

^{35}Cl EFG tensors were calculated from structural models obtained from DFT-TS* geometry optimizations (see below). Magnetic shielding tensors were calculated with the gauge-including projector augmented wave approach (Charpentier, 2011; Pickard & Mauri, 2001; Profeta *et al.*, 2003). Conversion between the magnetic shielding and chemical shift scales was accomplished through the following procedures: (i) ^{35}Cl shifts were referenced to NaCl(s) [$\delta(^{35}Cl)$ = 0.0 ppm, $\sigma(^{35}Cl)$ = 995.7 ppm]; (ii) ^{7}Li shifts were referenced to 1.0 M LiCl(aq) [$\delta(^{7}Li)$ = 0.0 ppm] using calculations on LiCl(s) [$\delta(^{7}Li)$ = −1.1 ppm, $\sigma(^{7}Li)$ = 90.8 ppm]; (iii) ^{23}Na shifts were referenced to 0.1 M NaCl(aq) [$\delta(^{23}Na)$ = 0.0 ppm] using calculations on NaCl(s) [$\delta(^{23}Na)$ = 7.0 ppm, $\sigma(^{23}Na)$ = 553.0 ppm]; (iv) ^{133}Cs shifts were referenced to 1.0 M CsCl(aq) [$\delta(^{133}Cs)$ = 0.0 ppm] using calculations on CsCl(s) [$\delta(^{133}Cs)$ = 223.2 ppm, $\sigma(^{133}Cs)$ = 5650.4 ppm]. Euler angles describing the relative orientations of the EFG and CS tensors were extracted from the *CASTEP* output files using *EFGShield* (Adiga *et al.*, 2007) and correspond to the $ZY'Z''$ convention (Adiga *et al.*, 2007; Pincherle, 1958; Mehring, 1983).

2.8. Molecular mechanics calculations

Molecular mechanics geometry optimizations were performed using the *FORCITE* module within *Materials Studio 2020*. These structural refinements employed the COMPASS III force field (Sun, 1998; Akkermans *et al.*, 2021) and an atom-based summation method for all interaction energies (*i.e.* electrostatic, van der Waals and hydrogen bonding). The molecular mechanics geometry optimizations were performed using the following convergence thresholds: 2×10^{-6} kcal mol^{-1} for energy, 10^{-3} kcal mol^{-1} Å^{-1} for forces and 10^{-6} Å for structural displacement.

2.9. Initial structure identification

Synchrotron PXRD patterns were indexed using the *X-Cell* algorithm (Neumann, 2003), as implemented in the *REFLEX* powder indexing module of *Materials Studio 2020*, to determine the unit-cell parameters. Subsequent Pawley refinement assisted in identifying the most probable space group (Pawley, 1981). Unit cells were then populated with the constituent atoms in the appropriate stoichiometric ratios (according to the stoichiometries determined by a combination of multinuclear

SSNMR, indexing of PXRD, TGA/DSC and chemical intuition based on reaction stoichiometries) and subjected to a molecular mechanics calculation using *FORCITE*. The structures of these MCCs were subjected to a series of alternating *REFLEX* refinements and *CASTEP* geometry optimizations until a single structural model consistent with both methods was achieved. The *CASTEP* geometry-optimized structural model was then submitted for Rietveld refinement.

2.10. Structure solution *via* Rietveld refinement

All structural solutions and Rietveld refinements were conducted using the synchrotron PXRD data. The resulting structural models were optimized in *FOX* (Favre-Nicolin & Černý, 2002). The suggested space groups were verified or adjusted as necessary. The space group with the highest symmetry that accurately describes the PXRD data was chosen throughout. Non-standard settings of monoclinic space groups were chosen when their monoclinic angles were found to be close to 90°. The optimized structures served as a starting model for *GSAS* (Toby & Von Dreele, 2013). Initially, urea was refined as a rigid body, but towards the end of the refinement all molecules were freely refined. In the case of NaCl:urea·H_2O, NaCl was added as a second phase in the refinement and was determined as 0.6% of the total weight (see Section 3.2.2 for further details).

3. Results and discussion

3.1. Mechanochemical syntheses

Mechanochemical syntheses (NG and LAG) using several alkali metal chlorides (*M*Cl, *M* = Li, Na, K, Rb or Cs) and urea as starting reagents were attempted, but only three MCCs were successfully produced: NaCl:urea·H_2O, CsCl:urea and LiCl:urea (see Table S1 for a summary of ball milling experiments), which were confirmed by PXRD (Fig. 1; also see Fig. S1 in the supporting information for PXRD patterns for solid products of unsuccessful syntheses). NaCl:urea·H_2O, which was previously generated by slow evaporation from H_2O (Müller *et al.*, 2008), was here prepared *via* LAG using 10 µl of TEA. Comparison of the experimental and simulated PXRD patterns indicates a small amount of unreacted NaCl (determined by ^{23}Na SSNMR to be *ca* 5% *w*/*w*, see below). By contrast, the novel CsCl:urea and LiCl:urea MCCs were prepared mechanochemically *via* NG, with their PXRD patterns showing no evidence of educts or impurity phases. Initial trials revealed that all three MCCs could be prepared in 40 min, a significant improvement over growing crystals from solution, which can take several days to weeks. Remarkably, NaCl:urea·H_2O and CsCl:urea can be made significantly faster *via* LAG using TEA, with optimized syntheses taking only 5 min to yield pure products (Figs. S2 and S3). The mechanochemical synthesis of LiCl:urea was not optimized because of sample deliquescence, with shorter milling times resulting in residual educts detectable by PXRD.

Despite their simple composition, these three MCCs proved challenging to prepare. The formation of NaCl:urea·H_2O was found to be highly dependent upon the pH of the water. Syntheses involving deionized (DI) water, which has a pH $\simeq$ 5.0–5.5 due to the dissolution of CO_2(g), always resulted in significant excesses of NaCl; we posit that this is likely to be due to carbonic acid in the DI water that deters MCC formation. To confirm this, four ball milling trials, conducted with (i) 0.1 M HNO_3 in DI water (pH $\simeq$ 1), (ii) neat DI water (pH $\simeq$ 5.5), (iii) Kirkland Signature bottled water (pH $\simeq$ 6) and (iv) 10 µl TEA in 18 µl DI water (pH $\simeq$ 11), showed that with increasing pH less NaCl educt is present in the ball milled products (Fig. S4). However, the use of bottled water with minimal atmospheric exposure results in the fewest impurities,

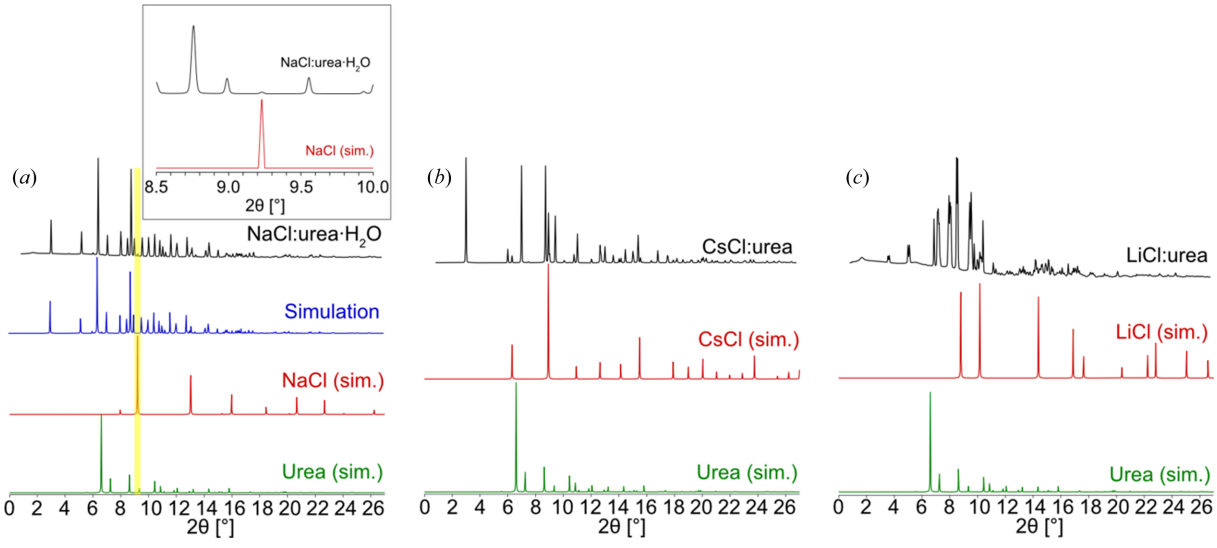

Figure 1
Experimental synchrotron PXRD patterns of (*a*) NaCl:urea·H_2O [with the inset showing evidence of NaCl(s) impurity at $2\theta = 9.22°$], (*b*) CsCl:urea and (*c*) LiCl:urea. Powder patterns are shown in black, with simulated PXRD patterns of the educts, urea and *M*Cl salts, shown in green and red, respectively. In panel (*a*), a simulated PXRD pattern (in blue) based on the known structure of NaCl:urea·H_2O is shown for comparison (Müller *et al.*, 2008). No evidence of residual educts is observed in the PXRD patterns of CsCl:urea and LiCl:urea.

thus indicating that the pH and alkalinity of the water used for synthesis is crucial in preparing products with high purity. The TGA/DSC scan of NaCl:urea·H_2O indicates MCC decomposition with an onset temperature of *ca* 50°C, followed by loss of water at *ca* 110°C [Fig. S5(*a*)]. As such, DSC indicates that NaCl:urea·H_2O is unstable under ambient conditions, whereas TGA confirms that it is a monohydrate. The instability of NaCl:urea·H_2O was further explored using ^{23}Na NMR (see below).

Since CsCl:urea was assumed to be a hydrate, its initial preparation occurred similarly to NaCl:urea·H_2O, using LAG with one equivalent of H_2O. The resulting PXRD pattern for the LAG product (Fig. S6) indicated the formation of a novel MCC and no leftover CsCl. However, TGA/DSC analysis [Fig. S5(*b*)] showed no evidence of water loss prior to the decomposition of the MCC at *ca* 200°C. As this indicated CsCl:urea to be anhydrous, this compound was also prepared *via* NG (without water). PXRD confirmed the NG product to be the same phase (Fig. S7).

Preparation of LiCl:urea involves reagents and a final product that are both hygroscopic. The mixture resulting from ball milling appeared as a wet grey paste. PXRD of the product revealed the presence of a significant amount of unreacted LiCl. As water was suspected to be the culprit, in a next attempt the reagents were filled into the milling jar in a drybox (N_2 atmosphere, <0.1% RH). The milling jar was wrapped with Teflon tape to exclude air and moisture during subsequent ball milling under ambient conditions. PXRD revealed the resulting product to be a novel MCC without impurities. TGA/DSC [Fig. S5(*c*)] revealed minor losses of water at *ca* 50 and 130°C, prior to decomposition of the product at *ca* 240°C. Because these losses were small in comparison to those observed for NaCl:urea·H_2O, they are attributed to the removal of surface water. This suggests LiCl:urea also is anhydrous.

We note that our failure to produce MCCs involving K^+ and Rb^+ is unsurprising in the light of previous work by Shemchuk *et al.* (2020), who proposed that the ratio between the ionic radii of the cation and anions plays a role in cocrystallization and dictates the type of crystal packing. They observed that the K^+/Cl^- ionic radius ratio is too large to form a 1:1 MCC and too small to form a 1:2 MCC. This is likely to be true for the case of Rb^+ as well.

3.2. Multinuclear SSNMR spectroscopy

3.2.1. ^{35}Cl SSNMR spectroscopy

^{35}Cl SSNMR spectra (Fig. 2) were acquired at two magnetic fields (9.4 and 21.1 T) to aid in the precise measurement of the EFG and CS tensors, since the broadening of CT patterns scales with B_0^{-1} and B_0 for the SOQI and CSA, respectively

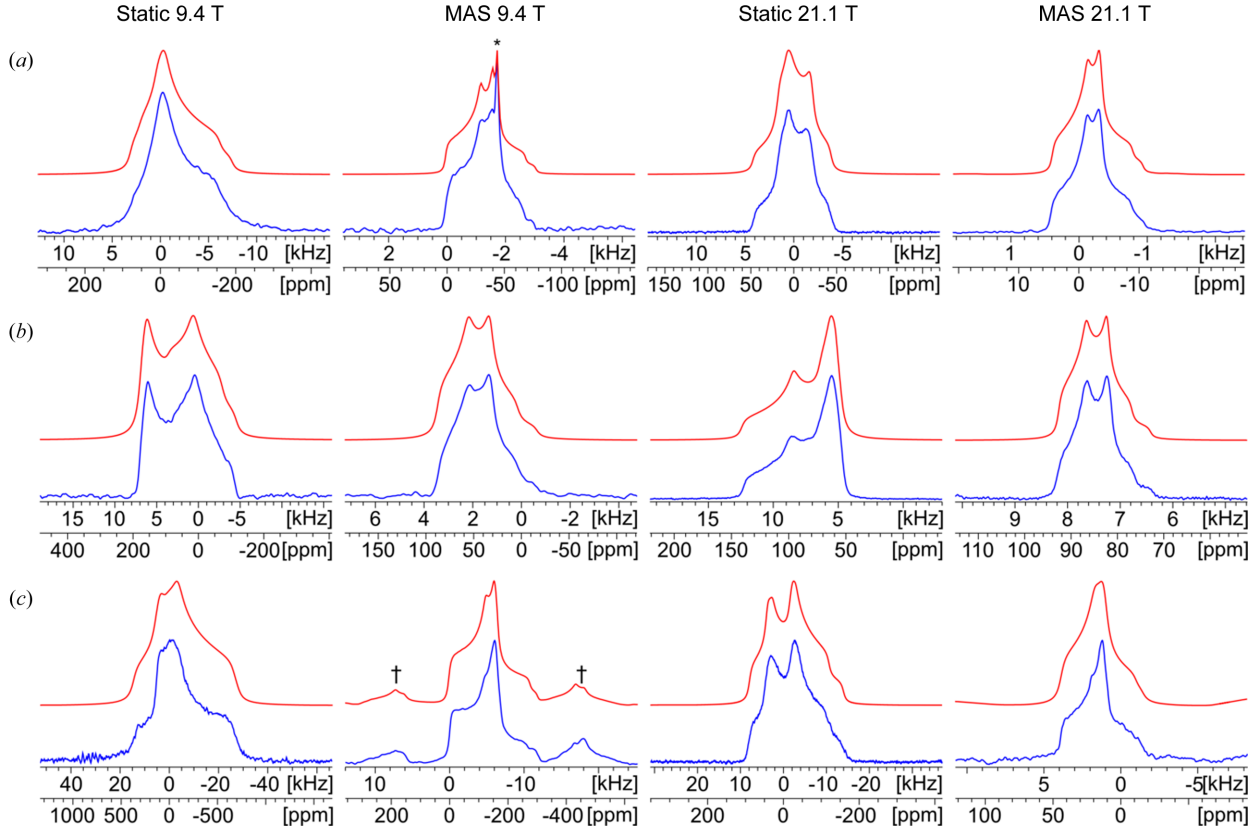

Figure 2
Experimental ^{35}Cl{^{1}H} SSNMR spectra for (*a*) NaCl:urea·H_2O, (*b*) CsCl:urea and (*c*) LiCl:urea (lower traces, blue), with corresponding analytical simulations (upper traces, red). Spectra were acquired at two fields (B_0 = 9.4 and 21.1 T) under static and MAS conditions (ν_{rot} = 10–12 kHz). Spinning sidebands are indicated by dagger symbols (†). In the MAS spectrum of NaCl:urea·H_2O acquired at 9.4 T, a peak at δ_{iso} = −41.11 ppm (indicated by an asterisk, *) indicates a small amount of residual NaCl.

(Vega, 2010; Baugher *et al.*, 1969; Kentgens, 1997). ^{35}Cl MAS NMR spectra allow for accurate determination of C_Q, η_Q and the isotropic chemical shift δ_{iso}, since the effects of CSA on the relatively narrow CT patterns are completely or partially averaged at high enough MAS rates (ν_{rot} = 10–12 kHz herein), leaving only the partially averaged effects of the SOQI. These parameters aid in fitting the static CT powder patterns, along with the span (Ω) and skew (κ) of the CS tensor and the Euler angles defining the relative orientation of the EFG and CS tensors (α, β and γ) (see Table 1 for definitions of these parameters).

In all cases, the ^{35}Cl NMR spectra feature single broad CT patterns, indicating no residual educts or impurity phases, with the exception of the MAS NMR spectrum of NaCl:urea·H_2O acquired at 9.4 T. In that case, a sharp peak is observed at *ca* −41.1 ppm, corresponding to a small amount of unreacted NaCl(s) (see discussion in Section 3.2.2 on quantification *via* measurement of integrated intensities and Rietveld refinement). Each CT powder pattern is indicative of a single crystallographically and magnetically distinct chloride ion in each crystal structure. In the case of NaCl:urea·H_2O, this is in accordance with the reported crystal structures (Müller *et al.*, 2008), whereas for LiCl:urea and CsCl:urea, this information is valuable for determining and refining their crystal structures (see below).

3.2.2. Alkali metal SSNMR spectroscopy

To investigate other quadrupolar NMR handles that might be useful for NMRX investigations and detection of educts and/or impurity phases, MAS NMR spectra of three alkali metal isotopes were acquired (Fig. 3). In each of the alkali metal NMR spectra, the QI manifests differently, due to the distinct nuclear spin quantum numbers and relatively small nuclear quadrupole moments. Acquisition of static spectra for these nuclides is generally not necessary, since ^{23}Na and ^{7}Li tend to have very small CSAs (with powder patterns largely dominated by quadrupolar effects), ^{133}Cs generally has small values of C_Q and moderate CSAs (see below), and acquisition of their MAS spectra is facile.

The ^{23}Na (I = 3/2) MAS spectrum features two patterns: a broad pattern dominated by the effects of the SOQI and a sharp peak at δ_{iso}(^{23}Na) = 7 ppm, corresponding to the Na^+ cation site in the NaCl:urea·H_2O MCC and the NaCl educt, respectively. Since CT-selective $\pi/2$ pulses were used for acquisition of ^{23}Na NMR spectra, the integrated peak intensities only provide approximate quantification of the amount of residual NaCl educt, since precise quantification would require significantly lower radio frequency pulses (Vega, 2010; Kentgens, 1997; Samoson & Lippmaa, 1983). Nonetheless, this fact, along with the use of long calibrated recycle delays in ^{23}Na SSNMR experiments, allows us to measure the integrated intensities of the sharp peaks and CT patterns, providing an estimation of 5 ± 2% *w*/*w* residual NaCl. Rietveld refinement of the synchrotron PXRD pattern revealed the crystalline NaCl to amount to 0.6 wt%. There are several possible explanations that account for the discrepancy in the quantification of NaCl in the sample, the simplest being that the samples for the NMR and synchrotron PXRD experiments are from different batches and therefore have different amounts of residual NaCl.

By contrast, the ^{133}Cs and ^{7}Li MAS NMR spectra are different, with neither exhibiting a broad CT pattern. The ^{133}Cs (I = 7/2) MAS NMR spectrum of CsCl:urea has a single sharp CT peak flanked by a series of sharp spinning sidebands, which is indicative of a single magnetically distinct Cs^+ site. Analysis reveals the presence of a substantial CSA (*i.e.* a CS tensor with a span Ω = 235 ppm) and a very small C_Q, with the spinning sidebands largely arising from the influence of the former. Finally, the ^{7}Li (I = 3/2) SSNMR spectrum of LiCl:urea features a sharp CT peak that is flanked by many spinning sidebands arising from the 3/2 ↔ 1/2 and −1/2 ↔ −3/2 satellite transitions (STs), which are broadened by the first-order QI and indicative of a single Li^+ cation in the asymmetric unit. There is no clear evidence of any ^{7}Li resonances corresponding to residual LiCl(s) or LiCl(aq), which have values of δ_{iso}(^{7}Li) = −1.1 and 0.0 ppm, respectively (Meyer *et al.*, 2005).

3.2.3. ^{23}Na SSNMR for monitoring of the decomposition of NaCl:urea·H_2O

In preliminary ^{23}Na MAS experiments at room temperature, changes observed in the ^{23}Na SSNMR spectra over time

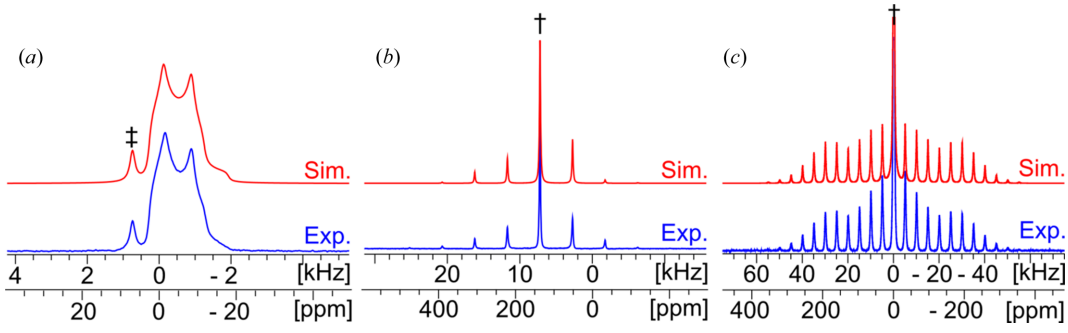

Figure 3
Experimental ^{23}Na, ^{133}Cs and ^{7}Li SSNMR spectra of (*a*) NaCl:urea·H_2O, (*b*) CsCl:urea and (*c*) LiCl:urea (lower traces, blue), with corresponding analytical simulations (upper traces, red). Spectra were acquired at 9.4 T under MAS conditions (ν_{rot} = 5–10 kHz). Isotropic peaks in panels (*b*) and (*c*) are labelled with dagger symbols (†). In the ^{23}Na spectrum in panel (*a*), a small amount of residual NaCl(s) is detected at δ_{iso} = 7 ppm, indicated with a double-dagger symbol (‡).

suggest the gradual decomposition of NaCl:urea·H_2O into its constituent components (NaCl, urea and water). Furthermore, samples removed from the rotor revealed (i) a gradual change from a white crystalline powder to a grey paste and (ii) a narrow 'bore hole' in the sample along the rotor axis, which is typically an indicator of water loss and/or sublimation. To monitor the decomposition of NaCl:urea·H_2O, a series of ^{23}Na MAS NMR spectra were collected (Fig. 4) using the following VT protocol:

(i) A stationary sample was cooled to a nominal temperature of 5°C and then the rotor was spun up to 10 kHz while maintaining this temperature (calibrations indicate an actual sample temperature of *ca* 8°C, due to frictional heating from MAS).

(ii) An initial ^{23}Na MAS NMR spectrum indicates that the sample is composed largely of NaCl:urea·H_2O with a small amount of NaCl(s).

(iii) The sample was heated to 30°C (calibrated temperature of *ca* 37°C under MAS) and ^{23}Na MAS NMR spectra (recycle delay of 37.5 s and 16 scans) were acquired every 10 min over a period of 3 h, leading to a total of 25 spectra. Over time, the ^{23}Na MAS NMR spectra [Fig. 4(*a*)] reveal the decomposition of NaCl:urea·H_2O into the starting educts, as monitored quantitatively *via* measurement of the integrated intensities of the patterns corresponding to NaCl:urea·H_2O and NaCl.

A plot of the mol.% of NaCl:urea·H_2O (as approximated from the ratio of the integrated intensities of the powder patterns of NaCl:urea·H_2O and NaCl) as a function of time [Fig. 4(*b*)] reveals a sigmoidal shape that may be indicative of autocatalytic behaviour (*i.e.* as NaCl:urea·H_2O decomposes, the release of H_2O serves to increase its rate of decomposition until a steady state is achieved). If this is the case, the induction period has a duration of *ca* 1200 s. Assuming the autocatalysis reaction follows an $A + B \rightarrow 2B$ reaction scheme, where A = NaCl:urea·H_2O and B = H_2O, then a decomposition rate k, which is assumed to be much larger than the reverse reaction, can be determined from the rate equation

$$R = -\frac{\mathrm{d}[A]}{\mathrm{d}t} = k[A][B]. \quad (1)$$

If $[A]_0$ and $[B]_0$ represent the concentrations (or mol.%) of A and B at the start of the reaction, then the total composition $[C]_0$ is defined as $[C]_0 = [A]_0 + [B]_0 = [A] + [B]$ at any time during the reaction; therefore, $[A]_0 - [A] = [B] - [B]_0$. Thus, the rate equation can be rewritten as

$$-\frac{\mathrm{d}[A]}{\mathrm{d}t} = k\{[A][A]_0 + [A]_0[B]_0 - [A]^2\}. \quad (2)$$

Equation (2) can be integrated with respect to $[A]$ to yield

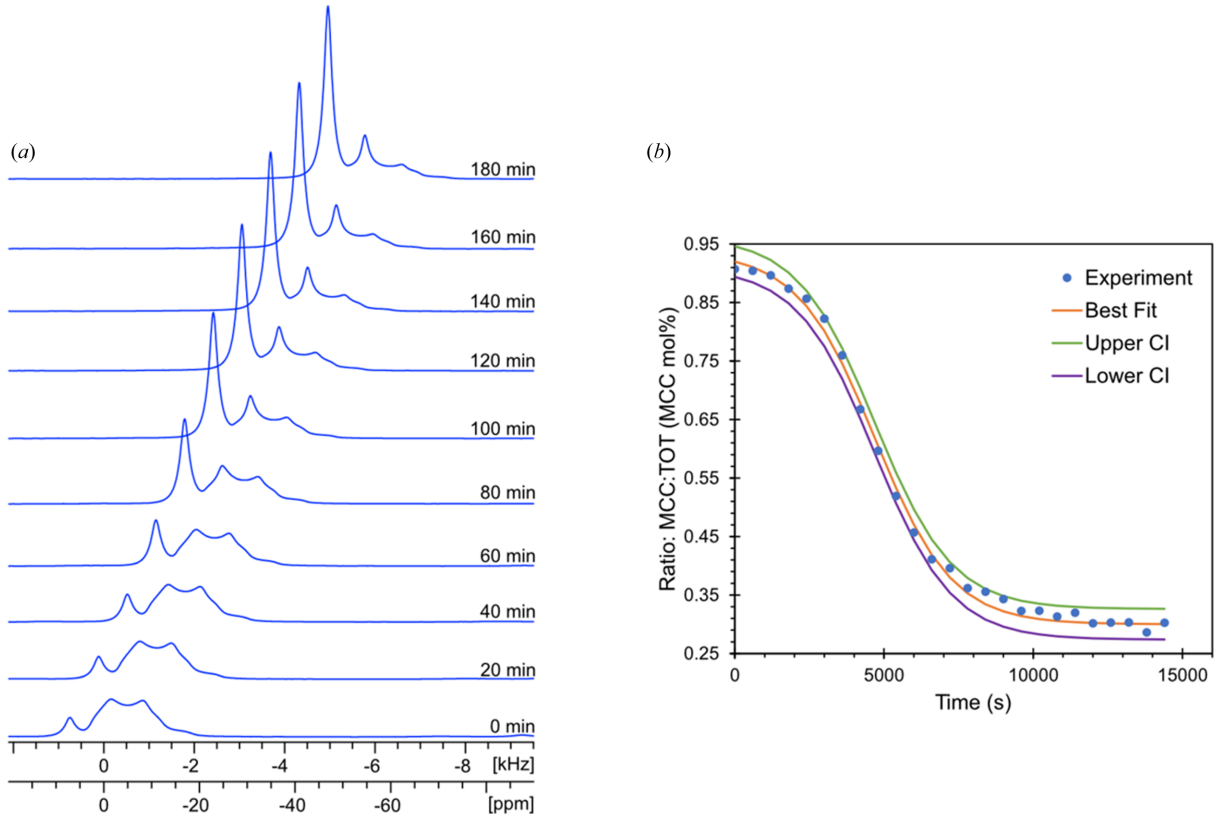

Figure 4
(*a*) Experimental ^{23}Na MAS NMR spectra of NaCl:urea·H_2O (ν_{rot} = 10 kHz) acquired at a fixed temperature of 30°C (calibrated sample temperature at ν_{rot} = 10 kHz is *ca* 37°C) over 3 h to monitor its degradation. (*b*) A plot of the mol.% of NaCl:urea·H_2O undergoing autocatalytic decomposition as a function of time (blue dots), along with a generalized reduced-gradient nonlinear least-squares fit using equation (4) (orange plot, see Section 3.2.3 for details). Upper and lower confidence intervals are indicated by the green and purple lines, respectively.

$$[A] = \frac{[A]_0 + [B]_0}{1 + ([B]_0/[A]_0)\exp\left\{([A]_0 + [B]_0)kt\right\}} = \frac{[C]_0}{1 + \left\{([C]_0 - [A]_0)/[A]_0\right\}\exp\left([C]_0\, kt\right)}. \quad (3)$$

Since $[A]_f$, the final mol.% of A, is not zero, the integral constant $F(C)$ is initially set equal to $[A]_f$:

$$[A] = \frac{[C]_0}{1 + \left\{([C]_0 - [A]_0)/[A]_0\right\}\exp\left([C]_0\, kt\right)} + F(C). \quad (4)$$

A fit of equation (4) using a generalized reduced-gradient nonlinear least-squares method yields excellent agreement with experiment, with a decomposition rate constant of $k = 1.22 \times 10^{-3}\ s^{-1}$ (Fig. 4). Additional fits treating the system with a combination of autocatalytic ($A + B \rightarrow 2B$) and direct ($A \rightarrow B$) reactions with two distinct rates of k_1 and k_2, respectively, failed to yield fits of satisfactory quality. A more rigorous determination of the autocatalytic rate constants featuring both measurements and fits at multiple temperatures is beyond the scope of the current work but is a clear point of interest for future studies of MCCs exhibiting either autocatalytic decomposition or growth (Julien *et al.*, 2020). We note that an analogous set of VT ^{35}Cl SSNMR experiments were not conducted, due to their much longer experimental times and the imperfect resolution of the two patterns corresponding to NaCl:urea·H_2O and NaCl.

3.2.4. SSNMR of other nuclides

There are several other potentially useful NMR handles for which data are not reported in this work. First, ^{13}C and ^{15}N SSNMR data (collected with ^{1}H–X cross-polarization MAS experiments) are not reported due to the very long $T_1(^1H)$ time constants, which would necessitate recycle delays of the order of 5.6 h, making these experiments impractical. This is in line with $T_1(^1H)$ constants reported by Taylor *et al.* (2007) for bulk urea. Second, ^{13}C and ^{15}N SSNMR spectra were thought to be of limited value, since significant differences between chemical shifts among the various solid forms were not expected (later chemical shielding calculations revealed differences of less than 1 ppm). Third, direct-excitation ^{13}C and ^{15}N experiments are similarly impractical, due to even longer $T_1(^{13}C)$ and $T_1(^{15}N)$ constants (this is especially problematic for ^{15}N, with its low natural abundance of ~0.37%). Finally, ^{14}N SSNMR experiments were not attempted due to the large C_Q value of 3.47 MHz in urea, lengthy experimental times even at very high fields and the necessity for deuteration of samples to maximize T_2^{eff} values (O'Dell & Ratcliffe, 2010).

3.3. NMR-guided crystallography

The NMRX approach used in this work implements a combination of Rietveld refinement of high-quality synchrotron PXRD data, multinuclear SSNMR of quadrupolar nuclei, thermal analysis and DFT calculations. Experimental synchrotron PXRD patterns were modelled and background corrected in the *BIOVIA Materials Studio* software package and indexed using the *REFLEX* module in *Materials Studio* (note that indexing the experimental synchrotron PXRD pattern is arguably the most challenging step in determining crystal structures of powdered samples, because slight variations in the number of peaks and positions can lead to significant deviations). The *X-Cell* algorithm was used to index the experimental synchrotron PXRD pattern and all potential solutions were subsequently subjected to a Pawley refinement to validate the indexing results. To generate an initial feasible structural model, the empty unit cells were populated with urea molecules, the appropriate ions and water molecules in a stoichiometric ratio in accordance with data from multinuclear SSNMR and TGA/DSC analyses. Bond lengths and angles were corrected using the *FORCITE* molecular mechanics module in *Materials Studio*. These structural models were refined iteratively using *REFLEX* refinements and *CASTEP* geometry optimizations until a consistent solution was obtained. The final *CASTEP* model was validated using *FOX*, which selected the space group with the highest possible symmetry for NaCl:urea·H_2O ($I2$) and CsCl:urea ($P\bar{4}2_1/m$) and the non-standard setting $I2/c$ with β near 90° for LiCl:urea (Table S4). The structural models were further optimized by Rietveld refinement in *GSAS*, initially using rigid-body constraints on urea and then by free refinement. Following this, H atoms were added to the structure in idealized positions. The resulting structures were subjected to final DFT-TS* geometry optimizations, enabling validation of the models by assessing the agreement between experimentally determined

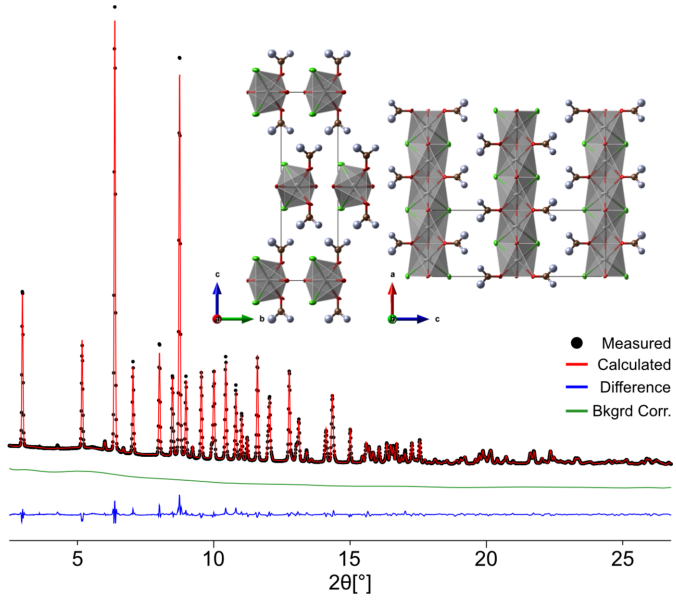

Figure 5
Rietveld plot for NaCl:urea·H_2O. Experimental data are shown in black and the calculated fit is shown in red. The difference plot is shown in blue and the background correction is shown in green. The inset (upper right) shows two views of the proposed crystal structure of NaCl:urea·H_2O. In the ball-and-stick model of the crystal structure, the different atoms are depicted as follows: carbon (brown), nitrogen (blue–grey), oxygen (red), chlorine (green) and sodium (grey). No hydrogen atoms are shown in these models.

^{35}Cl EFG tensors and those obtained from the final refined structures (see Section 3.4 for further details).

This NMRX approach was used to re-evaluate the structure of NaCl:urea·H_2O and to obtain solutions and refinements of the structures of CsCl:urea and LiCl:urea, which were hitherto unknown (see Fig. S8 and Table S4 for relevant crystallographic data). NaCl:urea·H_2O crystallizes in the monoclinic $C2$ space group (No. 5, $Z = 4$, $Z' = 1$) with lattice parameters $a = 6.4948$ Å, $b = 5.2446$ Å, $c = 17.3761$ Å, $\beta = 90.138°$ and $V = 591.874$ Å^3, and is best described in the $I2$ setting where the β angle is close to 90°. The final Rietveld refinement [Fig. 5, and Fig. S8(*a*)] gives an excellent fit of the synchrotron PXRD data ($R_p = 2.73\%$, $R_{wp} = 3.18\%$, $R_{F2} = 5.9\%$) and stands in good agreement with the previously reported SCXRD structure (Müller *et al.*, 2008).

While the structure of NaCl:urea had been determined previously, CsCl:urea and LiCl:urea were unknown structures. The CsCl:urea MCC crystallizes in the tetragonal $P\bar{4}2_1/m$ space group (No. 113, $Z = 2$, $Z' = 1$), with unit-cell parameters $a = 5.796$ Å, $c = 8.614$ Å and $V = 289.375$ Å^3. The final solution of the Rietveld refinement [Fig. 6 and Fig. S8(*b*)] shows excellent agreement with experimental synchrotron PXRD patterns ($R_p = 3.1\%$, $R_{wp} = 2.1\%$, $R_{F2} = 2.9\%$). LiCl:urea [Fig. 7 and Fig. S8(*c*)] crystallizes in the monoclinic $C2/c$ space group (No. 15, $Z = 16$, $Z' = 2$) with lattice parameters $a = 14.4063$ Å, $b = 8.867$ Å, $c = 14.5611$ Å, $\beta = 91.219°$ and $V = 1695.976$ Å^3, in the non-standard setting $I2/c$, where the β angle is close to 90° and a relation to a tetragonal net is apparent. The final Rietveld refinement solution shows good agreement with the experimental synchrotron PXRD patterns ($R_p = 1.9\%$, $R_{wp} = 2.6\%$, $R_{F2} = 4.4\%$).

Interestingly, while both NaCl:urea·H_2O and CsCl:urea MCCs exhibit only one alkali metal ion and one Cl^- ion in the asymmetric unit, as demonstrated by their respective NMR spectra, LiCl:urea nominally contains two sets of crystallographically distinct Li^+ and Cl^- species. A closer analysis suggests that the structure might best be described in the tetragonal space group $I4_1/a$, which would imply only one type of metal and halide ion. However, refinement of the crystal structure in this space group led to high displacement parameters (the average experimental structure in this space group is shown in Table S4).

The crystal structure for NaCl:urea·H_2O can be described as a layered structure consisting of alternating layers of *M*Cl, urea and water (Fig. 5, inset). The Na^+ ions are in six-coordinate environments, coordinated to two Cl^- ions, two O atoms from water molecules and two O atoms from urea molecules. These layers are stacked along the crystallographic c axis with the urea molecules directed at each other in a zigzag fashion. Similarly, the crystal structure for CsCl:urea features a layered structure consisting of CsCl and urea, with layers stacked along the crystallographic c axis and the urea molecules oriented in a zigzag fashion (Fig. 6, inset). However, the Cs^+ ions are in eight-coordinate environments, forming bonds to four Cl^- ions and four O atoms from urea molecules. Lastly, the crystal structure for LiCl:urea adopts an arrangement analogous to analcime (Yokomori & Idaka, 1998): the Li^+ ions are in four-coordinate environments featuring two

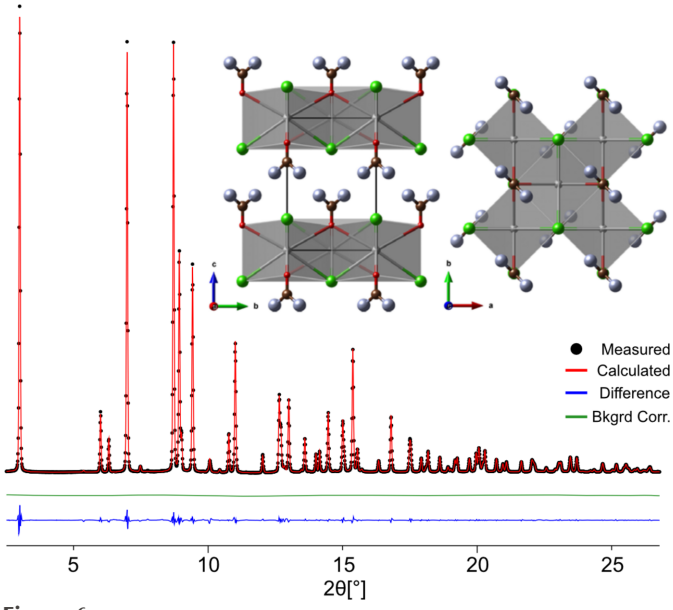

Figure 6
Rietveld plot for CsCl:urea. Experimental data are shown in black and the calculated fit is shown in red. The difference plot is shown in blue and the background correction is shown in green. The inset (upper right) shows two views of the proposed crystal structure of CsCl:urea. In the ball-and-stick model of the crystal structure, the different atoms are depicted as follows: carbon (brown), nitrogen (blue–grey), oxygen (red), chlorine (green) and caesium (grey). No hydrogen atoms are shown in these models.

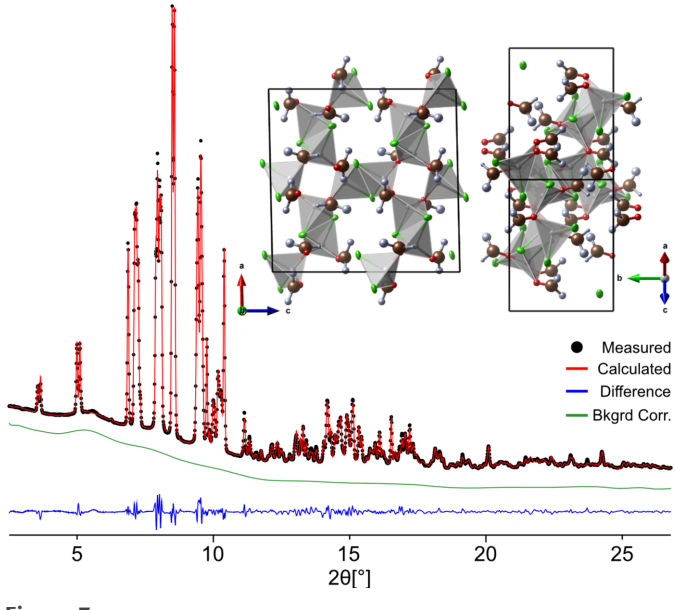

Figure 7
Rietveld refinement for LiCl:urea. Experimental data are shown in black and the calculated fit is shown in red. The difference plot is shown in blue and the background correction is shown in green. The inset (upper right) shows two views of the proposed crystal structure of LiCl:urea. In the ball-and-stick model of the crystal structure, the different atoms are depicted as follows: carbon (brown), nitrogen (blue–grey), oxygen (red), chlorine (green) and lithium (grey). No hydrogen atoms are shown in these models.

Cl^- ions and two O atoms from urea molecules, with the polyhedra alternating between edge-sharing and corner-sharing along the crystallographic normal (*n*) axis (Fig. 7, inset).

Of the three MCCs described herein, the crystal structure of LiCl:urea raises some questions. The best solution (*i.e.* lowest energy) is consistent with the lower-symmetry subgroup *I*2/*c* of the tetragonal space group $I4_1/a$. DFT-TS* geometry optimizations in the latter space group failed to converge. While the structural topology is consistent with a tetragonal net, the experimental observation and computational confirmation of a monoclinic space group with $\beta = 91.2°$ implies a slight unit-cell deformation of the tetragonal unit cell, perhaps due to molecular-level dynamics (see the video in the supporting information). Since the structure with $\beta = 91.2°$ has a symmetry-equivalent structure with $\beta = 88.8°$, it is possible to refine a structure in the $I4_1/a$ space group, albeit with high displacement parameters and the assumption that both structures are present in equal amounts. This is confirmed in part by the highly anisotropic displacement ellipsoids of the Cl^- ions (Fig. 7). From the diffraction data alone, it is not possible to ascertain the presence of dynamic or static disorder. However, the dynamics of the urea molecules in MCCs can significantly impact the SSNMR powder patterns of ^{35}Cl, ^{14}N, ^{2}H and quadrupolar alkali metal nuclides.

To explore the possibility of dynamics influencing the observed ^{35}Cl tensor parameters for either LiCl:urea or CsCl:urea, we measured VT ^{35}Cl spectra at two temperatures, 25 and −95°C, at 18.8 T (Fig. S9). We elected to focus on LiCl:urea and CsCl:urea since the synchrotron PXRD data and Rietveld refinements suggested the possible presence of dynamics in these materials. We found that there are only minimal differences in the appearances of the spectra between these two temperatures, suggesting that molecular motions in this temperature range have little impact on the observed ^{35}Cl EFG and CS tensor parameters.

We also gave consideration to acquiring ^{6}Li SSNMR spectra in the hope of resolving the two lithium shifts, which are not resolved in the ^{7}Li SSNMR spectrum, since the crystallographically unique Li^+ sites exist in almost identical environments. As lithium has one of the smallest chemical shift ranges, it is very common not to be able to resolve such sites in ^{7}Li SSNMR spectra – in fact, our DFT calculations indicate that the lithium shifts differ by only 0.019 ppm and would not be differentiated by either ^{7}Li or ^{6}Li SSNMR (the chemical shift dispersion for ^{7}Li is 2.64× that of ^{6}Li at the same field). Furthermore, ^{6}Li SSNMR spectra are generally of higher resolution than those of ^{7}Li, due to the lower quadrupole moment and reduced homonuclear dipolar couplings, but require much longer acquisition times (at natural abundance) due to low receptivity $R(^6\text{Li})/R(^7\text{Li}) \simeq 1/30$ and very long $T_1(^6\text{Li})$ times.

3.4. DFT calculations and EFG tensor orientations

Quantum chemical computations are key in elucidating relationships between NMR interaction tensors and molecular-level structure (Holmes *et al.*, 2020; Holmes *et al.*, 2022*a*; Vojvodin *et al.*, 2022; Holmes & Schurko, 2018; Holmes *et al.*, 2017). Here, we consider a comparison of the experimentally measured ^{35}Cl quadrupolar parameters with the ^{35}Cl EFG tensors and orientations obtained from DFT calculations. The ^{35}Cl EFG tensors are obtained from DFT calculations on the final refined structural models from the combination of Rietveld refinements and DFT-TS* geometry optimizations (see Section 3.3) (Holmes *et al.*, 2020). There is reasonably good agreement between the experimental and calculated ^{35}Cl EFG and CS tensors in all cases (Table 1) (Holmes *et al.*, 2022*a*; Holmes *et al.*, 2022*b*; Vojvodin *et al.*, 2022; Abdulla *et al.*, 2023).

There are well established relationships between the ^{35}Cl EFG tensors of chloride ions and hydrogen bonding in organic solids (the relationships between chlorine CS tensors and bonding are not straightforward, so further discussion is largely restricted to the EFG tensors) (Hildebrand *et al.*, 2014; Hamaed *et al.*, 2008; Holmes *et al.*, 2022*a*). A hydrogen bond is defined as having an $H\cdots Cl^-$ distance $r(H\cdots Cl^-)$ of 2.6 Å or less (Desiraju & Steiner, 2001), whereas a short contact is defined as a hydrogen bond with $r(H\cdots Cl^-) \lesssim 2.2$ Å. $H\cdots Cl^-$ short contacts exert the most influence on the ^{35}Cl EFG tensor parameters and orientations, with many organic HCl salts exhibiting values of C_Q ranging from *ca* 5 to 9 MHz in cases with one or two short contacts. The exceptions to this rule are $H\cdots Cl^-$ contacts involving H_2O molecules, which present challenges for accurate calculations of ^{35}Cl EFG tensors (Holmes *et al.*, 2022*b*). These relationships have not been explored for MCCs featuring both chloride ions and alkali metal cations. Furthermore, for the three structural models herein, there are no short contacts (only between three and five hydrogen bonds) and relatively small magnitudes of C_Q (Table 2). Nonetheless, it is worth investigating the orientations of the ^{35}Cl EFG tensors to determine if they are constrained by local symmetry, local bonds and/or crystallographic symmetry elements.

We now consider the relationships between the ^{35}Cl EFG tensor orientations and local hydrogen-bonding environments of the chloride ions in the three MCCs (Fig. 8). The chloride ions in NaCl:urea·H_2O are defined by a single crystallographic position, are not located in crystallographic symmetry mirror planes or on rotational axes (because of the low symmetry of the space group), and feature five hydrogen bonds involving urea (four) and water (one). Two monodentate urea molecules have the shortest $H\cdots Cl^-$ bonds of $r(H\cdots Cl^-) = 2.383$ and 2.475 Å with an $H\cdots Cl^-\cdots H$ angle of $\angle(H\cdots Cl\cdots H) = 129.3°$, and the single bidentate urea has $r(H\cdots Cl^-) = 2.486$ and 2.503 Å with $\angle(H\cdots Cl^-\cdots H) = 54.1°$. The largest component of the EFG tensor, V_{33}, is oriented approximately perpendicular to the bidentate $H\cdots Cl^-\cdots H$ plane, with V_{22} approximately in the plane and bisecting the $\angle(H\cdots Cl^-\cdots H)$ plane. V_{33} is calculated to be negative [*i.e.* C_Q is positive, since $Q(^{35}\text{Cl}) = -8.165$ fm^2], meaning the EFG diminishes along this axis moving away from the nucleus (note that the sign of C_Q cannot be determined from ^{35}Cl SSNMR spectra, but can be calculated and used for interpreting relationships between structure and EFG tensors). The negative and positive signs of V_{33} and V_{22}, respectively, as well as their orientations, are

Table 2
H···Cl$^-$ hydrogen bonds ($\lesssim$ 2.6 Å), contact angles and calculated ^{35}Cl EFG tensors.

MCC	Hydrogen-bond type†	H···Cl$^-$ distance‡ (Å)	*X*···Cl$^-$ distance§¶ (Å)	*X*—H···Cl$^-$ angle‖¶ (°)	δ_{iso} (ppm)	C_Q (MHz)	η_Q
NaCl:urea·H_2O	NH···Cl$^-$	2.383	3.332	169.9	−15	1.64	0.49
	NH···Cl$^-$	2.475	3.42	168.5			
	NH···Cl$^-$	2.486	3.373	153.7			
	NH···Cl$^-$	2.503	3.385	152.7			
	HOH···Cl$^-$	2.240	3.133	163.0			
CsCl:urea	NH···Cl$^-$	2.340	3.297	176.5	82	−1.77	0.69
	NH···Cl$^-$	2.340	3.297	176.5			
	NH···Cl$^-$	2.494	3.383	154.1			
	NH···Cl$^-$	2.494	3.383	154.1			
LiCl:urea (Cl1)	NH···Cl$^-$	2.366	3.322	173.9	−10	2.94	0.90
	NH···Cl$^-$	2.419	3.35	163.1			
	NH···Cl$^-$	2.577	3.468	154.7			
LiCl:urea (Cl2)	NH···Cl$^-$	2.354	3.312	175.0	−10	2.94	0.90
	NH···Cl$^-$	2.431	3.347	159.8			
	NH···Cl$^-$	2.613	3.496	153.2			

† The functional group involved in the H···Cl$^-$ hydrogen bond (*e.g.* NH···Cl$^-$ and HOH···Cl$^-$ signify hydrogen bonds with an amine functional group or water molecule and a chloride ion, respectively), as obtained from calculations on structures refined at the RPBE-TS* level. ‡ H···Cl$^-$ hydrogen bonds ($\leq$ 2.6 Å), as determined from crystal structures refined at the DFT-TS* level. § Distance between the chloride ion and the hydrogen-bond donor atom. ¶ *X* represents the atom bonded to hydrogen (*i.e.* N or O). ‖ Angle between the hydrogen-bond donor atom, the hydrogen atom and the chloride anion.

consistent with numerous predictions for similar H···Cl$^-$···H arrangements (Hildebrand *et al.*, 2014; Hamaed *et al.*, 2008; Holmes *et al.*, 2022*a*; Vojvodin *et al.*, 2022).

In contrast to NaCl:urea·H_2O, the chloride ions in CsCl:urea are positioned in crystallographic mirror planes and on a twofold rotational axis, with one set of H···Cl$^-$ hydrogen bonds from monodentate urea ligands reflected through the mirror plane [r(H···Cl$^-$) = 2.340 Å], one set of bidentate H···Cl$^-$ hydrogen bonds in the mirror plane [r(H···Cl$^-$) = 2.494 Å and ∠(H···Cl$^-$···H) = 53.6°] and four identical Cs···Cl$^-$ contacts [r(H···Cl$^-$) = 3.514 Å]. V_{11} and V_{22} are positioned in the crystallographic mirror plane, with V_{33} oriented parallel to the mirror plane and perpendicular to the bidentate H···Cl$^-$···H plane. Opposite to the case of NaCl:urea·H_2O, V_{33} is positive and V_{11} bisects the ∠(H···Cl$^-$···H) plane.

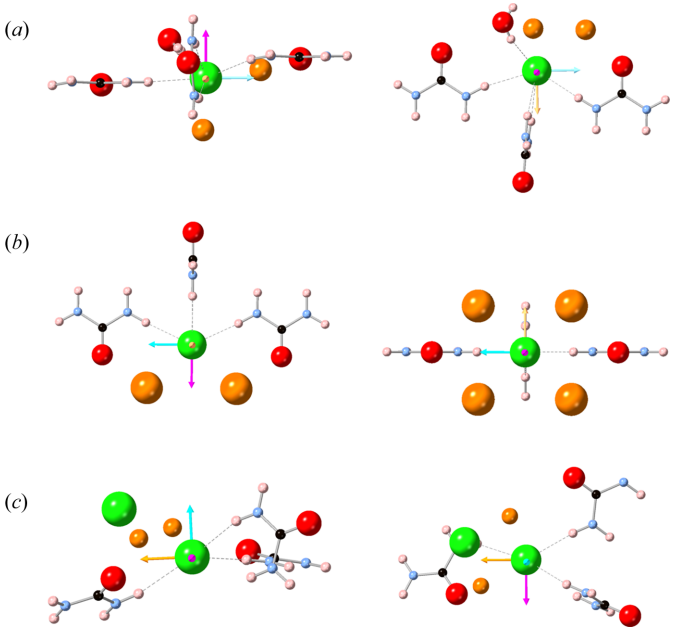

Figure 8
^{35}Cl EFG tensor orientations (two views for each system) for (*a*) NaCl:urea·H_2O, (*b*) CsCl:urea and (*c*) LiCl:urea, obtained from calculations on structural models determined from Rietveld refinement and geometry optimization at the RPBE-TS* level. The H···Cl$^-$ hydrogen bonds (<2.6 Å) are shown as black dashed lines. The orientations of the three principal components of the ^{35}Cl EFG tensors are shown as arrows in magenta (V_{11}), yellow (V_{22}) and cyan (V_{33}).

LiCl:urea, in the monoclinic description, displays two crystallographically distinct chloride ions that are not associated with any symmetry operations in *I*2/*c* (either local or otherwise). Their local environments are almost identical, with three hydrogen bonds ranging from r(H···Cl$^-$) = 2.354 Å to r(H···Cl$^-$) = 2.613 Å and two Li···Cl contacts (<2.417 Å). In this system, which features the largest magnitudes of C_Q in the *M*Cl:urea·*x*H_2O series, the values of C_Q and η_Q are calculated to be almost identical for the two sites [C_Q(Cl1) = 2.99 MHz, η_Q(Cl1) = 0.90, and C_Q(Cl2) = 2.94 MHz, η_Q(Cl2) = 0.90], with V_{33} (which is negative) located approximately in an H···Cl$^-$···H plane formed by the shortest and longest hydrogen bonds, with an angle of ∠(V_{33}—Cl$^-$···H) ≃ 51°.

Several conclusions arise from the comparison of experimentally measured and computationally derived ^{35}Cl EFG tensors and from consideration of their orientations: (i) even though the magnitudes of the QIs are small, the ^{35}Cl EFG tensor parameters and orientations are highly dependent on local symmetry, hydrogen bonds (number, length and moieties of origin) and crystallographic symmetry elements; and (ii) despite the absence of short H···Cl$^-$ contacts, the ^{35}Cl EFG tensors orient themselves in a manner consistent with those previously described in the literature (Hildebrand *et al.*, 2014; Hamaed *et al.*, 2008; Holmes *et al.*, 2022*b*; Vojvodin *et al.*, 2022; Abdulla *et al.*, 2023).

4. Conclusions

Herein, we have demonstrated novel mechanochemical routes to synthesize three MCCs of the form *M*Cl:urea·*x*H_2O (*x* = 0,

1) and conducted their structural characterization by integration of synchrotron PXRD, multinuclear SSNMR spectroscopy, Rietveld refinement and plane-wave DFT calculations. The MCCs described herein can be prepared mechanochemically with high purity and great rapidity relative to more conventional cocrystallization through slow evaporation from water.

The combination of PXRD and SSNMR analyses for the characterization of products of mechanochemical reactions proves to be extremely useful for rapid screening of products (as well as residual educts and/or impurities) and for the optimization of milling conditions (including milling time, milling media and pH of the milling liquid). ^{35}Cl SSNMR is well suited for the structural characterization of these MCCs, since ^{35}Cl EFG tensors are extremely sensitive to the smallest differences and/or changes in chloride ion environments, providing a powerful means of examining H$\cdots$Cl$^-$ bonding in organic solids.

Alkali metal NMR proves to be useful for identifying the number of unique crystallographic sites and for facile detection of educts and/or impurities; however, at present it appears to be of limited use for aiding in structural refinements of MCCs, since (i) their EFG tensors do not vary to the degree of those of ^{35}Cl EFG tensors, largely due to the unresponsiveness of the alkali metal valence electrons to hydrogen bonding; and (ii) ^{7}Li and ^{133}Cs spectra of Li^+ and Cs^+ ions in organic solids generally have C_Q values with very small magnitudes, which are challenging to calculate. Furthermore, it is possible that the dynamics of urea molecules in certain cases must be taken into account to make valid comparisons of experimental and calculated NMR interaction tensor data.

^{23}Na MAS NMR was key for identifying residual NaCl educt and proved to be beneficial for monitoring the degradation of NaCl:urea·H_2O and extracting a decomposition rate constant of $k = 1.22 \times 10^{-3}$ s^{-1}.

Finally, NMRX-guided Rietveld refinements, aided by comparison of ^{35}Cl EFG tensors determined from experiment and computation, were used to resolve the structure of NaCl:urea·H_2O and solve the novel structures of CsCl:urea and LiCl:urea. As a result, the insight garnered from this quadrupolar NMR-guided crystallography (*i.e.* QNMRX) study of relatively simple MCCs with alkali metal cations and chloride anions will be useful for directing future structural predictions and/or refinements of similar MCCs, and perhaps even new solid forms of pharmaceutical cocrystals featuring a wide range of pharmaceuticals, cations, anions and other organic coformers.

Acknowledgements

Dr Victor Terskikh is thanked for technical support and access to the 900 MHz NMR spectrometer, which was provided by the National Ultrahigh-Field NMR Facility for Solids (Ottawa, Canada).

Conflict of interest

The authors declare that they have no known competing financial interests or personal relationships that could have appeared to influence the work reported in this paper.

Funding information

We thank Florida State University, the National High Magnetic Field Laboratory and the State of Florida, for support in the form of a startup grant. Robert Schurko is grateful for research support from Florida State University and the National High Magnetic Field Laboratory (NHMFL), which is funded by the National Science Foundation Cooperative Agreement (grant Nos. DMR-1644779 and DMR-2128556) and by the State of Florida. A portion of this research used resources provided by the X-ray Crystallography Center at the FSU Department of Chemistry and Biochemistry (FSU075000XRAY). The XRD experiments used resources of the Advanced Photon Source Beamline 17-BM (XRD) at Argonne National Laboratory, which is an Office of Science User Facility operated for the US Department of Energy (DOE) Office of Science and was supported by the US DOE (contract No. DE-AC02-06CH11357 to Sanjaya Senanayake and Wenqian Xu). This research used resources of the Advanced Light Source, a US DOE Office of Science User Facility (contract No. DE-AC02-05CH11231 to Sanjaya Senanayake and Wenqian Xu). The National Ultrahigh-Field NMR Facility for Solids (Ottawa, Canada) is a national research facility funded by the Canada Foundation for Innovation, the Ontario Innovation Trust, Recherche Québec, the National Research Council of Canada and Bruker BioSpin, and is managed by the University of Ottawa (https://www.nmr900.ca). The following funding is also acknowledged: KU Leuven (grant No. SIONA C14/22/099 to Christine Kirschhock and Eric Breynaert); European Research Council (grant No. 834134 WATUSO to Eric Breynaert); Fonds Wetenschappelijk Onderzoek (grant No. V401721N to Eric Breynaert); Hercules Foundation (award No. AKUL/13/21 to Eric Breynaert); Vlaamse regering (grant No. I001321N to Eric Breynaert); Departement Economie, Wetenschap en Innovatie *via* the Hermes Fund (grant No. AH.2016.134 to Eric Breynaert); McGill University (award to Tomislav Friščić); Natural Sciences and Engineering Research Council of Canada (grant No. RGPIN-2017-06467 to Tomislav Friščić); Leverhulme International Professorship (award to Tomislav Friščić); University of Birmingham (award to Tomislav Friščić).

References

Abdulla, L. M., Peach, A. A., Holmes, S. T., Dowdell, Z. T., Watanabe, L. K., Iacobelli, E. M., Hirsh, D. A., Rawson, J. M. & Schurko, R. W. (2023). *Cryst. Growth Des.* **23**, 3412–3426.
Abraham, A., Apperley, D. C., Gelbrich, T., Harris, R. K. & Griesser, U. J. (2011). *Can. J. Chem.* **89**, 770–778.
Adiga, S., Aebi, D. & Bryce, D. L. (2007). *Can. J. Chem.* **85**, 496–505.
Akkermans, R. L. C., Spenley, N. A. & Robertson, S. H. (2021). *Mol. Simul.* **47**, 540–551.
Alkan, F., Holmes, S. T. & Dybowski, C. (2017). *J. Chem. Theory Comput.* **13**, 4741–4752.
Andersen, J. & Mack, J. (2018). *Green Chem.* **20**, 1435–1443.
Ashbrook, S. E. & McKay, D. (2016). *Chem. Commun.* **52**, 7186–7204.
Babu, N. J. & Nangia, A. (2011). *Cryst. Growth Des.* **11**, 2662–2679.

Baias, M., Widdifield, C. M., Dumez, J.-N., Thompson, H. P. G., Cooper, T. G., Salager, E., Bassil, S., Stein, R. S., Lesage, A., Day, G. M. & Emsley, L. (2013). *Phys. Chem. Chem. Phys.* **15**, 8069.

Baig, R. B. N. & Varma, R. S. (2012). *Chem. Soc. Rev.* **41**, 1559–1584.

Baugher, J. F., Taylor, P. C., Oja, T. & Bray, P. J. (1969). *J. Chem. Phys.* **50**, 4914–4925.

Bonhomme, C., Gervais, C., Babonneau, F., Coelho, C., Pourpoint, F., Azaïs, T., Ashbrook, S. E., Griffin, J. M., Yates, J. R., Mauri, F. & Pickard, C. J. (2012). *Chem. Rev.* **112**, 5733–5779.

Bruker (2020). *TopSpin Software.* Version 4.1. Bruker BioSpin, Ettlingen, Germany.

Bryce, D. L. (2017). *IUCrJ*, **4**, 350–359.

Bryce, D. L., Gee, M. & Wasylishen, R. E. (2001). *J. Phys. Chem. A*, **105**, 10413–10421.

Bryce, D. L. & Sward, G. D. (2006). *Magn. Reson. Chem.* **44**, 409–450.

Bryce, D. L., Sward, G. D. & Adiga, S. (2006). *J. Am. Chem. Soc.* **128**, 2121–2134.

Buchsbaum, C. & Schmidt, M. U. (2007). *Acta Cryst.* B**63**, 926–932.

Burgess, K. M. N., Xu, Y., Leclerc, M. C. & Bryce, D. L. (2014). *Inorg. Chem.* **53**, 552–561.

Burgess, K. M. N. N., Perras, F. A., Lebrun, A., Messner-Henning, E., Korobkov, I. & Bryce, D. L. (2012). *J. Pharm. Sci.* **101**, 2930–2940.

Cerreia Vioglio, P., Chierotti, M. R. & Gobetto, R. (2017). *Adv. Drug Deliv. Rev.* **117**, 86–110.

Charpentier, T. (2011). *Solid State Nucl. Magn. Reson.* **40**, 1–20.

Cherginets, V. L., Baumer, V. N., Galkin, S. S., Glushkova, L. V., Rebrova, T. P. & Shtitelman, Z. V. (2006). *Inorg. Chem.* **45**, 7367–7371.

Cherukuvada, S., Kaur, R. & Guru Row, T. N. (2016). *CrystEngComm*, **18**, 8528–8555.

Clark, S. J., Segall, M. D., Pickard, C. J., Hasnip, P. J., Probert, M. I. J. J., Refson, K. & Payne, M. C. (2005). *Z. Kristallogr. Cryst. Mater.* **220**, 567–570.

Desiraju, G. & Steiner, T. (2001). *The weak hydrogen bond*. Oxford University Press.

Eichele, K. & Wasylishen, R. E. (2021). *WSolids1*. Version 1.21.7. Universität Tübingen, Germany. http://anorganik.uni-tuebingen.de/klaus/soft/index.php?p=wsolids1/.

Favre-Nicolin, V. & Černý, R. (2002). *J. Appl. Cryst.* **35**, 734–743.

Friščić, T., Childs, S. L., Rizvi, S. A. A. & Jones, W. (2009). *CrystEngComm*, **11**, 418–426.

Friščić, T. & Jones, W. (2010). *J. Pharm. Pharmacol.* **62**, 1547–1559.

Friščić, T., Mottillo, C. & Titi, H. M. (2020). *Angew. Chem. Int. Ed.* **59**, 1018–1029.

Gadade, D. D. & Pekamwar, S. S. (2016). *Adv. Pharm. Bull.* **6**, 479–494.

Ganesan, V. & Girirajan, K. S. (1987). *Solid State Phys.* **28**, 73–79.

Hamaed, H., Pawlowski, J. M., Cooper, B. F. T. T., Fu, R., Eichhorn, S. H. & Schurko, R. W. (2008). *J. Am. Chem. Soc.* **130**, 11056–11065.

Hammer, B., Hansen, L. B. & Nørskov, J. K. (1999). *Phys. Rev. B*, **59**, 7413–7421.

Harris, K. D. M. (2011). *Peptide-Based Mater.* **310**, 133–177.

Harris, R. K., Wasylishen, R. E. & Duer, M. J. (2009). Editors. *NMR crystallography*. Chichester: John Wiley & Sons.

Hartman, J. D., Day, G. M. & Beran, G. J. O. O. (2016). *Cryst. Growth Des.* **16**, 6479–6493.

Hildebrand, M., Hamaed, H., Namespetra, A. M., Donohue, J. M., Fu, R., Hung, I., Gan, Z. & Schurko, R. W. (2014). *CrystEngComm*, **16**, 7334–7356.

Hirsh, D. A., Holmes, S. T., Chakravarty, P., Peach, A. A., DiPasquale, A. G., Nagapudi, K. & Schurko, R. W. (2019). *Cryst. Growth Des.* **19**, 7349–7362.

Hirsh, D. A., Rossini, A. J., Emsley, L. & Schurko, R. W. (2016). *Phys. Chem. Chem. Phys.* **18**, 25893–25904.

Hirsh, D. A., Su, Y., Nie, H., Xu, W., Stueber, D., Variankaval, N. & Schurko, R. W. (2018). *Mol. Pharm.* **15**, 4038–4048.

Hodgkinson, P. (2020). *Prog. Nucl. Magn. Reson. Spectrosc.* **118–119**, 10–53.

Holmes, S. T., Hook, J. M. & Schurko, R. W. (2022*a*). *Mol. Pharm.* **19**, 440–455.

Holmes, S. T., Iuliucci, R. J., Mueller, K. T. & Dybowski, C. (2017). *J. Chem. Phys.* **146**, 064201.

Holmes, S. T. & Schurko, R. W. (2018). *J. Phys. Chem. C*, **122**, 1809–1820.

Holmes, S. T., Vojvodin, C. S. & Schurko, R. W. (2020). *J. Phys. Chem. A*, **124**, 10312–10323.

Holmes, S. T., Vojvodin, C. S., Veinberg, N., Iacobelli, E. M., Hirsh, D. A. & Schurko, R. W. (2022*b*). *Solid State Nucl. Magn. Reson.* **122**, 101837.

Howard, J. L. L., Cao, Q. & Browne, D. L. (2018). *Chem. Sci.* **9**, 3080–3094.

Ievina, A., Straumanis, M. & Karlsons, K. (1938). *Z. Phys. Chem.* **40B**, 146–150.

James, S. L., Adams, C. J., Bolm, C., Braga, D., Collier, P., Friščić, T., Grepioni, F., Harris, K. D. M. M., Hyett, G., Jones, W., Krebs, A., Mack, J., Maini, L., Orpen, A. G., Parkin, I. P., Shearouse, W. C., Steed, J. W. & Waddell, D. C. (2012). *Chem. Soc. Rev.* **41**, 413–447.

Johnston, K. E., Griffin, J. M., Walton, R. I., Dawson, D. M., Lightfoot, P. & Ashbrook, S. E. (2011). *Phys. Chem. Chem. Phys.* **13**, 7565.

Jones, W., Motherwell, W. D. S. & Trask, A. V. (2006). *MRS Bull.* **31**, 875–879.

Julien, P. A., Germann, L. S., Titi, H. M., Etter, M., Dinnebier, R. E., Sharma, L., Baltrusaitis, J. & Friščić, T. (2020). *Chem. Sci.* **11**, 2350–2355.

Kalakewich, K., Iuliucci, R., Mueller, K. T., Eloranta, H. & Harper, J. K. (2015). *J. Chem. Phys.* **143**, 194702.

Karimi-Jafari, M., Padrela, L., Walker, G. M. & Croker, D. M. (2018). *Cryst. Growth Des.* **18**, 6370–6387.

Kentgens, A. P. M. A. (1997). *Geoderma*, **80**, 271–306.

Klein, P., Dedecek, J., Thomas, H. M., Whittleton, S. R., Klimes, J., Brus, J., Kobera, L., Bryce, D. L. & Sklenak, S. (2022). *J. Phys. Chem. C*, **126**, 10686–10702.

Kuminek, G., Cao, F., Bahia de Oliveira da Rocha, A., Gonçalves Cardoso, S. & Rodríguez-Hornedo, N. (2016). *Adv. Drug Deliv. Rev.* **101**, 143–166.

Leroy, C. & Bryce, D. L. (2018). *Prog. Nucl. Magn. Reson. Spectrosc.* **109**, 160–199.

Lim, G. K., Fujii, K., Harris, K. D. M. & Apperley, D. C. (2011). *Cryst. Growth Des.* **11**, 5192–5199.

Luedeker, D., Gossmann, R., Langer, K. & Brunklaus, G. (2016). *Cryst. Growth Des.* **16**, 3087–3100.

Margetić, D. & Štrukil, V. (2016). *Mechanochemical organic synthesis*, pp. 1–54. Amsterdam: Elsevier.

Martineau, C. (2014). *Solid State Nucl. Magn. Reson.* **63–64**, 1–12.

Martineau, C., Cadiau, A., Bouchevreau, B., Senker, J., Taulelle, F. & Adil, K. (2012). *Dalton Trans.* **41**, 6232.

Martineau, C., Senker, J. & Taulelle, F. (2014). *Annual reports on NMR spectroscopy*, Vol. 82, pp. 1–57. Amsterdam: Elsevier.

McCusker, L. B., Von Dreele, R. B., Cox, D. E., Louër, D. & Scardi, P. (1999). *J. Appl. Cryst.* **32**, 36–50.

McNamara, D. P., Childs, S. L., Giordano, J., Iarriccio, A., Cassidy, J., Shet, M. S., Mannion, R., O'Donnell, E. & Park, A. (2006). *Pharm. Res.* **23**, 1888–1897.

Meerten, S. G. J. van, Franssen, W. M. J. & Kentgens, A. P. M. (2019). *J. Magn. Reson.* **301**, 56–66.

Mehring, M. (1983). *Principles of high resolution NMR in solids*. Berlin, Heidelberg: Springer.

Meyer, B. M., Leifer, N., Sakamoto, S., Greenbaum, S. G. & Grey, C. P. (2005). *Electrochem. Solid-State Lett.* **8**, A145.

Mir, N. A., Dubey, R. & Desiraju, G. R. (2019). *Acc. Chem. Res.* **52**, 2210–2220.

Monkhorst, H. J. & Pack, J. D. (1976). *Phys. Rev. B*, **13**, 5188–5192.

Moudrakovski, I. L. (2013). *Annual reports on NMR spectroscopy*, Vol. 79, pp. 129–240. Amsterdam: Elsevier.

Müller, S., Schäfer, O. & Keller, E. (2008). *Acta Cryst.* C**64**, m300–m304.
Namespetra, A. M., Hirsh, D. A., Hildebrand, M. P., Sandre, A. R., Hamaed, H., Rawson, J. M. & Schurko, R. W. (2016). *CrystEngComm*, **18**, 6213–6232.
Neumann, M. A. (2003). *J. Appl. Cryst.* **36**, 356–365.
O'Dell, L. A. & Ratcliffe, C. I. (2010). *Chem. Commun.* **46**, 6774.
Pandey, M. K., Kato, H., Ishii, Y. & Nishiyama, Y. (2016). *Phys. Chem. Chem. Phys.* **18**, 6209–6216.
Pawlak, T., Jaworska, M. & Potrzebowski, M. J. (2013). *Phys. Chem. Chem. Phys.* **15**, 3137.
Pawley, G. S. (1981). *J. Appl. Cryst.* **14**, 357–361.
Peach, A. A., Hirsh, D. A., Holmes, S. T. & Schurko, R. W. (2018). *CrystEngComm*, **20**, 2780–2792.
Perras, F. A. & Paterson, A. L. (2024). *Solid State Nucl. Magn. Reson.* **131**, 101935.
Pfrommer, B. G., Côté, M., Louie, S. G. & Cohen, M. L. (1997). *J. Comput. Phys.* **131**, 233–240.
Pickard, C. J. & Mauri, F. (2001). *Phys. Rev. B*, **63**, 245101.
Pincherle, L. (1958). *Elementary theory of angular momentum*. New York: Wiley.
Pindelska, E., Sokal, A. & Kolodziejski, W. (2017). *Adv. Drug Deliv. Rev.* **117**, 111–146.
Profeta, M., Mauri, F. & Pickard, C. J. (2003). *J. Am. Chem. Soc.* **125**, 541–548.
Rice, C. M., Davis, Z. H., McKay, D., Bignami, G. P. M. M. M., Chitac, R. G., Dawson, D. M., Morris, R. E. & Ashbrook, S. E. (2020). *Phys. Chem. Chem. Phys.* **22**, 14514–14526.
Romao, C. P., Perras, F. A., Werner-Zwanziger, U., Lussier, J. A., Miller, K. J., Calahoo, C. M., Zwanziger, J. W., Bieringer, M., Marinkovic, B. A., Bryce, D. L. & White, M. A. (2015). *Chem. Mater.* **27**, 2633–2646.
Samoson, A. & Lippmaa, E. (1983). *Phys. Rev. B*, **28**, 6567–6570.
Schurko, R. W. & Jaroszewicz, M. J. (2015). *Encyclopedia of inorganic and bioinorganic chemistry*, pp. 1–56. Chichester: John Wiley & Sons.
Sene, S., Bouchevreau, B., Martineau, C., Gervais, C., Bonhomme, C., Gaveau, P., Mauri, F., Bégu, S., Mutin, P. H., Smith, M. E. & Laurencin, D. (2013). *CrystEngComm*, **15**, 8763.
Shemchuk, O., Grepioni, F. & Braga, D. (2020). *Cryst. Growth Des.* **20**, 7230–7237.
Smalley, C. J. H., Hoskyns, H. E., Hughes, C. E., Johnstone, D. N., Willhammar, T., Young, M. T., Pickard, C. J., Logsdail, A. J., Midgley, P. A. & Harris, K. D. M. A. (2022). *Chem. Sci.* **13**, 5277–5288.
Soss, S. E., Flynn, P. F., Iuliucci, R. J., Young, R. P., Mueller, L. J., Hartman, J., Beran, G. J. O. & Harper, J. K. (2017). *ChemPhysChem*, **18**, 2225–2232.
Sun, H. (1998). *J. Phys. Chem. B*, **102**, 7338–7364.
Szell, P. M. J. & Bryce, D. L. (2016*a*). *J. Phys. Chem. C*, **120**, 11121–11130.
Szell, P. M. J. & Bryce, D. L. (2016*b*). *Concepts Magn. Reson. Part A*, **45**, 1–11.
Szell, P. M. J. & Bryce, D. L. (2020). *Annual reports on NMR spectroscopy*, Vol. 84, pp. 97–152. Amsterdam: Elsevier.
Szell, P. M. J., Rehman, Z., Tatman, B. P., Hughes, L. P., Blade, H. & Brown, S. P. (2023). *ChemPhysChem*, **24**, e202200558.
Tan, D. & Friščić, T. (2018). *Eur. J. Org. Chem.* **2018**, 18–33.
Tan, D. & García, F. (2019). *Chem. Soc. Rev.* **48**, 2274–2292.
Tan, D., Loots, L. & Friščić, T. (2016). *Chem. Commun.* **52**, 7760–7781.
Taulelle, F. (2009). *Encyclopedia of magnetic resonance*, edited by R. K. Harris, R. E. Wasylishen & M. J. Duer, pp. 1–14. Chichester: John Wiley & Sons.
Taylor, R. E., Bacher, A. D. & Dybowski, C. (2007). *J. Mol. Struct.* **846**, 147–152.
Tkatchenko, A. & Scheffler, M. (2009). *Phys. Rev. Lett.* **102**, 073005.
Toby, B. H. (2006). *Powder Diffr.* **21**, 67–70.
Toby, B. H. & Von Dreele, R. B. (2013). *J. Appl. Cryst.* **46**, 544–549.
Varma, R. S. (2014). *Green Chem.* **16**, 2027.
Vega, A. J. (2010). *Encyclopedia of magnetic resonance*, edited by D. M. Grant & R. K. Harris, pp. 3869–3888. Chichester: John Wiley & Sons.
Vogt, F. G., Williams, G. R. & Copley, R. C. B. B. (2013). *J. Pharm. Sci.* **102**, 3705–3716.
Vojvodin, C. S., Holmes, S. T., Watanabe, L. K., Rawson, J. M. & Schurko, R. W. (2022). *CrystEngComm*, **24**, 2626–2641.
Watts, A. E., Maruyoshi, K., Hughes, C. E., Brown, S. P. & Harris, K. D. M. M. (2016). *Cryst. Growth Des.* **16**, 1798–1804.
Weyna, D. R., Shattock, T., Vishweshwar, P. & Zaworotko, M. J. (2009). *Cryst. Growth Des.* **9**, 1106–1123.
Widdifield, C. M., Farrell, J. D., Cole, J. C., Howard, J. A. K. K. & Hodgkinson, P. (2020). *Chem. Sci.* **11**, 2987–2992.
Widdifield, C. M., Perras, F. A. & Bryce, D. L. (2015). *Phys. Chem. Chem. Phys.* **17**, 10118–10134.
Wijesekara, A. V., Venkatesh, A., Lampkin, B. J., VanVeller, B., Lubach, J. W., Nagapudi, K., Hung, I., Gor'kov, P. L., Gan, Z. & Rossini, A. J. (2020). *Chem. A Eur. J.* **26**, 7881–7888.
Wu, G. & Zhu, J. (2012). *Prog. Nucl. Magn. Reson. Spectrosc.* **61**, 1–70.
Xu, Y., Southern, S. A., Szell, P. M. J. J. & Bryce, D. L. (2016). *CrystEngComm*, **18**, 5236–5252.
Yates, J. R., Dobbins, S. E., Pickard, C. J., Mauri, F., Ghi, P. Y. & Harris, R. K. A. (2005). *Phys. Chem. Chem. Phys.* **7**, 1402.
Yates, J. R., Pickard, C. J. & Mauri, F. (2007). *Phys. Rev. B*, **76**, 024401.
Yokomori, Y. & Idaka, S. (1998). *Microporous Mesoporous Mater.* **21**, 365–370.